

FINAL REPORT

OTHER TRANSACTION AGREEMENT #DTRS56-02-T-0005

BETWEEN

**WITTEN TECHNOLOGIES, INC.
35 MEDFORD STREET, SUITE 306
SOMERVILLE, MA 02143**

AND

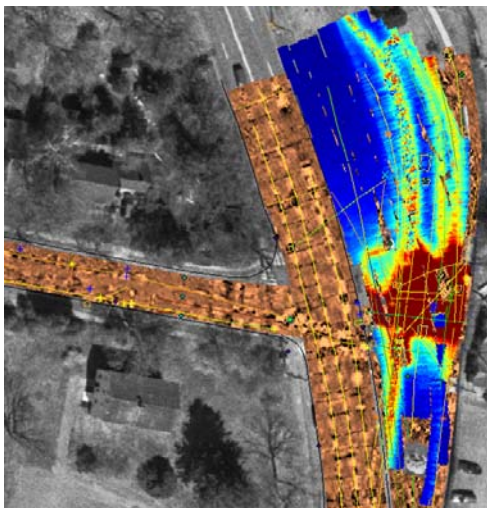
**THE U.S. DEPARTMENT OF TRANSPORTATION
RESEARCH AND SPECIAL PROGRAMS ADMINISTRATION
400 7TH STREET, S.W.
WASHINGTON, D.C. 20590-0001.**

CONCERNING

“DIGITAL MAPPING OF BURIED PIPELINES WITH A DUAL ARRAY SYSTEM”

(OCTOBER 1, 2002 – DECEMBER 31, 2004)

DISTRIBUTION STATEMENT: Public Version.



**Submitted by:
Witten Technologies Inc.
35 Medford Street
Suite 306
Somerville, MA 02143
USA**

www.wittentech.com

TABLE OF CONTENT

1	INTRODUCTION	4
1.1	Outline of document.....	4
1.1.1	Units and Abbreviations	5
1.2	Project overview: Technical background, goals, and applications	7
1.2.1	Radar waves in soil	7
1.2.2	Electromagnetic induction in soil.....	8
1.2.3	A Mobile Platform for High-Resolution Underground Mapping	10
1.3	Applications of the dual-array system	11
1.4	Project history and accomplishments	12
2	EMI ARRAY EXPERIMENTAL PROTOTYPE.....	13
2.1	Magnetic field sensors	13
2.1.1	Vector magnetometers: 3-axis induction sensors (coil pods)	13
2.2	Magnetic field sources	14
2.2.1	Clamp-on Transmitter (current injection source).....	14
2.2.2	On-board Transmitter (induction source)	15
2.3	Data acquisition system	16
2.3.1	Requirements and specifications	17
2.3.2	Comparison of DAQ systems	18
2.4	Positioning system	19
2.5	Sensor Platform and Vehicle	21
2.6	Software	21
2.6.1	Acquisition Software	22
2.6.2	Preprocessing Software	23
2.6.3	Positioning and Geometry Software.....	23
2.6.4	Inversion Software.....	24
2.6.5	Mapping Software and GIS	24
3	FIELD TESTS	26
3.1	Sensor Tests: Apr 2003 Cape Cod.....	26
3.2	Sensor Tests: May 2003 Con Edison West End Avenue and 59th Street.....	26
3.3	Array Mock Up Test: Newton, Massachusetts	27

- 3.4 First large-scale survey: November 2003, Southern Connecticut (RWA) 28
- 3.5 Resurvey of Southern Connecticut site (RWA) with modified sensors 29
- 3.6 Final Field Test: July 2004 Elmsford, NY (Con Edison)..... 30
- 3.7 Field Test Assessment..... 32
- 4 COMMERCIALIZATION ISSUES 34
 - 4.1 Dual-array engineering prototype 34
 - 4.1.1 Sensors: Radar and EMI arrays 34
 - 4.1.2 Data acquisition 35
 - 4.1.3 Positioning system 35
 - 4.1.4 Vehicle 35
 - 4.1.5 Data processing and data management system..... 36
 - 4.2 Cost-benefit analysis 36
 - 4.2.1 Cost Analysis of 3D Mapping with Dual Array System..... 37
 - 4.3 Commercialization Strategy 39
- 5 FINANCIAL SUMMARY 40
- 6 ACKNOWLEDGEMENT 44
- 7 REFERENCES 45
- APPENDIX A: U. S. DOT NEWS RELEASE 47
- APPENDIX B: UTILITY LOCATING MARKETS: ONE-CALL SYSTEM AND SUE 49
- APPENDIX C: PHYSICS OF THE DUAL-ARRAY SYSTEM 51
- APPENDIX D: CART IMAGING SYSTEM 60
- APPENDIX E: INVERSION MODELS FOR INDUCTIVE PIPE LOCATING..... 62
- APPENDIX F: DATA FILE FORMATS 70

1 Introduction

This document is the final report for

Other Transaction Agreement #DTRS56-02-T-0005,
“Digital mapping of buried pipelines with a dual array system”,

between

Witten Technologies, Inc.
295 Huntington Avenue, Suite 203
Boston, MA 02115

and

THE U.S. DEPARTMENT OF TRANSPORTATION
RESEARCH AND SPECIAL PROGRAMS ADMINISTRATION
400 7TH STREET, S.W.
WASHINGTON, D.C. 20590-0001.

The project carried out under this agreement, which was informally called the “Dual Array Project” (the term we will use in this report), was part of the research efforts at the Office of Pipeline Safety at U.S. DOT, and was one of seven contracts awarded by competitive proposals in October 2002 in the area of damage prevention and leak detection (U.S. DOT News Release, November 15, 2002, APPENDIX A). The technical goal of the Dual Array Project was to develop new technology for non-invasive mapping of buried pipelines, down to depths of 10 meters or more, using modern electromagnetic sensors and signal processing. A major proposed innovation in the work was integration of the sensor arrays and software into a mobile system capable of mapping underground utility networks (and other buried infrastructure) efficiently over large areas. Ultimately, the goal is to have a non-invasive system that can produce an accurate infrastructure map of an entire urban or suburban utility network in digital form. This goal requires the development of new geophysical remote sensing technologies to create underground images down to the depths of most buried utilities in the United States and the development of software to extract features from the images to create digital maps that can be archived electronically – for example, in Geographic Information Systems (GIS). Key components of each of these goals were developed and demonstrated during the Dual-Array Project.

The technical work in the Dual Array Project was done by Witten Technologies, Inc., with contributions from Electromagnetic Instruments, Inc. (a division of Schlumberger), in development of new magnetic field sensors, and from Seknion, Inc., in analysis of the final field tests and writing of the final report. Consolidated Edison Company of New York, Inc. and South Central Connecticut Regional Water Authority (RWA) collaborated on the major field tests. Con Edison was also a cost-sharing partner on the agreement with U.S. DOT and helped with setting the technical goals for the project. The full documentation for the project consists of this final report and the nine quarterly reports supplied to U.S. DOT during the course of the project, which started in October 2002 and finished in December 2004.

1.1 Outline of document

The final report is organized as follows. The first three sections summarize the main results of the technical work carried out during the Dual Array Project. The rest of this Introduction (Section 1) discusses the original technical concept and goals for the dual-array system and reviews briefly the history of the project and its accomplishments. The main new technology developed under the agreement

with U.S. DOT was an array of highly-sensitive vector magnetometers – electromagnetic induction (EMI) sensors which can measure magnetic fields over a broad range of frequencies – along with software to invert the measurements to determine the location of the buried pipes. The sensors developed in this project are the most sensitive mobile instruments available for measuring magnetic fields at frequencies in the kilohertz (kHz) range that can penetrate soil to the depths needed. The full sensor array, consisting of 16 vector magnetometers operating between 1 Hz and 100 kHz, is the first instrument of its kind capable of mapping magnetic fields at street level accurately over such a broad range of frequencies. The EMI sensor array is one component of the dual-array system. The other component is intended to be a ground-penetrating radar (GPR) array developed earlier by Witten Technologies and marketed under the brand name *CART Imaging System*. APPENDIX D describes the CART system.

Section 2 describes the different hardware and software components of the prototype EMI array, while Section 3 describes the key laboratory and field tests of the new EMI sensors and of the full sensor array. (Other tests are described at length in the quarterly reports.) The field tests included two large surveys mapping portions of urban underground networks: one survey covering about 20 000 square feet was done in southern Connecticut for the South Central Connecticut Regional Water Authority; the other, covering nearly 40 000 square feet, was done in Elmsford (NY) for Con Edison. These sites were also surveyed by the commercial CART radar system so that the EMI data and radar images could be interpreted jointly to demonstrate the full potential of the dual-array concept. In particular, the final field test at Elmsford included all elements planned for a commercial dual-array system.

Section 4 covers issues related to a commercialization of technology developed in the Dual-Array project. These include improvements that should be made in developing an integrated dual-array system combining both radar and EMI arrays on a single platform. A cost estimate is given for development of an engineering prototype (ENP) dual-array system that could serve as a template for commercial production. This section also includes a preliminary cost-benefit analysis for a large-scale commercial mapping service using a dual-array system. At present, there is only a very small market for large-scale mapping of buried utilities, but this market could grow substantially within the next five years as demands increase for better management of the world's vast underground infrastructure. In discussing commercialization of the dual-array system, comparisons are made with the nationwide One-Call System and with the growing market for subsurface utility engineering (SUE). Section 4 concludes with a possible strategy and plan for a follow-on project to advance the dual-array system to the ENP level. Section 5 contains a financial summary of the project.

Several appendices cover some of the more technical issues related to the project's goals. The most important of these are APPENDICES B and C. APPENDIX B describes two utility locating markets, the One-Call System and SUE. APPENDIX C briefly reviews the physics of electromagnetic signals in soils and discusses the state-of-the-art and limits of current radar and EMI technology for remote sensing of the shallow subsurface.

1.1.1 Units and Abbreviations

We use SI (mks) units for all physical quantities, except for measurements of distances (locations or depths), since it is still convenient in the United States to use feet and inches in describing utility maps and configurations. When it is not cumbersome, we also give the metric equivalents for distances. We use standard abbreviations for these quantities, as indicated in the table below. We use the second (s) for units of time and hertz (Hz) for the unit of frequency, where $1 \text{ Hz} = 1 \text{ s}^{-1}$ (i.e., one cycle per second). We also use decibels (dB) to compare the amplitude S of a signal to a reference amplitude S_0 , where

$$\text{dB} = 20 \log_{10} (S/S_0) \quad (1)$$

For example, a signal amplitude of -20 dB indicates a signal with one-tenth the amplitude of the reference.

LENGTH AND TIME UNITS					
inch	in	2.54 cm	centimeter	cm	.393 in
foot	ft	30.47 cm	meter	m	3.28 ft
mile	mi	1.609 km	kilometer	km	.621 mi
second	s		Hertz	Hz	s ⁻¹
nanosecond	ns	10 ⁻⁹ s	GigaHertz	GHz	10 ⁹ Hz

Electromagnetic units

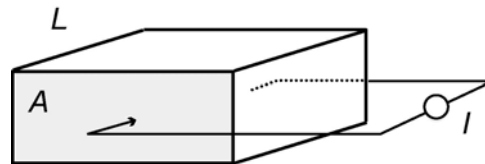
The basic SI units needed for a description of electromagnetic quantities measured by the dual-array system are the ampere (A) for current and the volt (V) for differences in potential. All other electromagnetic field quantities are combinations of these units with the meter and second. The SI unit for the electric field is volt/meter (V/m). The unit for the magnetic field is volt-second/meter² (V-s/m²), a quantity which is called the tesla (T). One tesla, however, represents a very large field strength for most engineering applications. For example, the magnetic field at a distance of 1 m from a long wire carrying 1 A of steady current is only 2×10^{-7} T or 0.2 microtesla (μ T). It is therefore common in engineering applications to use units of nanotesla (nT) for the magnetic field, where $1 \text{ nT} = 10^{-9} \text{ T}$. Another common unit for magnetic fields is the gauss (G), where $1 \text{ G} = 10^{-4} \text{ T}$. Units of gauss are common because the natural (static) magnetic field of the earth is about 0.5 G (or about 50 000 nT). In this report, we will use nanotesla (nT) as the units for magnetic field. The nanotesla is sometimes called the gamma (γ).

An important physical quantity for discussion of the physics of EM waves in soil is electrical resistance, which expresses the relationship between current and voltage in a resistor,

$$V = IR, \quad (2)$$

where V the voltage drop across the resistor carrying current I , and R is the resistance. The units of resistance are volt/ampere (V/A), also called ohm. Electrical resistance is a circuit property; the intrinsic material property that gives rise to electrical resistance is called electrical resistivity, which has units of ohm-m and is usually represented by the Greek symbol rho (ρ). The relationship between resistance and resistivity is illustrated in the figure below: If current I , distributed uniformly over a cross-sectional area A , flows a distance L along a block of material with resistivity ρ , then the resistance felt by the current is proportional to the resistivity of the material and to the length of the block and is inversely proportional to the cross-sectional area. That is,

$$R = \rho L/A \quad (3)$$



A related unit is the electrical conductivity, which is the inverse of electrical resistivity ($1/\rho$). Conductivity is usually represented by Greek sigma (σ) and has units of (ohm-m)⁻¹, also called siemens/m (S/m).

ELECTROMAGNETIC UNITS			
volt	V	potential difference	
ampere	A	current	
volt/m	V/m	electric field	
tesla	T	magnetic field	V-s/m ²
nanotesla	nT	magnetic field	10 ⁻⁹ T
ohm	Ω	(bulk) resistance	V/A
siemens	S	(bulk) conductance	A/V
resistivity	ρ	(intrinsic) resistance	ohm-m = m/S
conductivity	σ	(intrinsic) conductance	(ohm-m) ⁻¹ = S/m

1.2 Project overview: Technical background, goals, and applications

The technical goal of the Dual Array Project was to develop a non-invasive system for detecting, mapping, and inspecting buried steel and plastic pipelines by combining measurements from two sensor arrays: an array of ultra-wideband ground-penetrating radar antennas, operating at frequencies in the range from about 50 MHz to 1 GHz, and an array of broadband electromagnetic induction (EMI) sensors, operating at frequencies from about 50 Hz to 100 kHz. The electromagnetic spectrums in the two different frequency ranges – the radar regime (MHz) and the induction regime (kHz) – complement each other well in probing the shallow subsurface. This is illustrated schematically in FIGURE 1 and discussed briefly below. Different physical parameters dominate in the two regimes, generating diffusive behavior of electromagnetic signals in the induction regime and wavelike behavior in the radar regime. The transition between the two is determined by a parameter that depends on the ratio of the soil's electrical conductivity to the product of its permittivity (also called the dielectric constant) times the frequency of the electromagnetic signals. In most soils, this transition from inductive to wavelike behavior starts at frequencies of about 10 MHz and is usually complete by 50 MHz. APPENDIX C discusses in further detail the physics of radar and induction and develops the basic equations that can be used to analyze the capabilities of these two techniques for detecting and mapping buried objects.

1.2.1 Radar waves in soil

Ground-penetrating radar, also called “ground-probing radar” or GPR, uses a transmitting antenna to broadcast short pulses of electromagnetic energy into the ground and a receiving antenna to detect the echoes returning to the surface (FIGURE 1 left). In the radar regime, electromagnetic signals propagate in soil as a true wavefield, similar to radio waves in air (vacuum), which travel at the speed of light – approximately 300 000 000 m/s or about 1 ft/ns. The speed of radio waves in all materials, including soil, is less than the speed of light in vacuum; the reduction factor is called the material's index of refraction. For most soils, the index is in the range from about 2 to 4, which means that the speed of radio waves in typical soils is two to four times slower than in air. For example, in soil with an index of refraction of 3, radio waves travel at a speed of about 4 in/ns.

As radio waves penetrate into soil, radar echoes are generated by any object whose electrical properties contrast with those of the soil. Metal objects generate the strongest radar echoes, but nearly all other man-made materials, including plastics, cements, and ceramics can also generate detectable echoes. In addition, the boundary of a local region of soil whose properties differ from the “average”, such as an unusually wet patch, can also generate echoes. In fact, one of major difficulties in interpreting GPR is to

distinguish the radar echoes caused by the objects of interest (such as buried utility lines) from the background “clutter” of echoes generated by other objects in the subsurface. A technique that helps greatly with GPR interpretation is to scan the antennas over the ground, collecting data on a dense grid, so that the echoes can be processed into images showing the shapes and locations of buried objects. This process is called synthetic-aperture imaging and is the basis of the imaging radar in the CART system. The resolution of underground images created by synthetic-aperture GPR is limited mainly by the wavelength of radio waves in the soil, which is proportional to the speed of waves and inversely proportional to their frequency; that is,

$$\lambda = v/f, \quad (4)$$

where λ is the wavelength of the radio waves; v , the speed; and f , the frequency. The range of useful frequencies for GPR is about 50 MHz to 1 GHz. This range is determined by a number of factors, including new FCC rules limiting the power in certain frequency bands. The wavelength at 1 GHz of radio waves in soil with an index of 3 is about 4 in. The rule of thumb is that the maximum resolution is limited to about one-fourth of the (shortest) wavelength. For radio waves at 1 GHz, in soil with an index of 3, this rule of thumb gives a resolution of about 1 in. A more typical figure for GPR is a highest frequency of about 400 MHz, which gives a resolution of about 2.5 inches (10 cm).

The range of ground-penetrating radar in soil (its “depth of penetration”) is limited by two significant effects. The first is an exponential attenuation of the signal amplitude caused by absorption of the radio waves in material making up the soil. The intrinsic attenuation rate is proportional to the soil’s electrical conductivity (or inversely proportional to its resistivity). This intrinsic attenuation rate is very high for radio waves in soil; an approximate formula is

$$\alpha_{radar} \sim -1637 \sigma/n \text{ dB/m (radar attenuation rate)}, \quad (5)$$

where α_{radar} is the attenuation rate in dB/m, σ is the soil’s conductivity in S/m, and n is its index of refraction. Thus, for example radio waves traveling in soil with conductivity of 0.02 S/m (corresponding to a resistivity of 50 ohm-m) and an index of refraction of 3 decay at the rate of about -10 dB per meter of travel. Modern GPR systems have a dynamic range of about 60 dB, which means that the radio waves can travel only about 6 m in soil before becoming undetectable to the system (“falling off the radar screen”). This corresponds to a depth of penetration about 3 m for detecting buried objects with GPR, because the waves have to travel 3 m down to the object and 3 m back to the surface. For most soils, the conductivity is mainly determined by the presence of salt water either in the pore space or adhering to clay particles. Because of this, radar works best in dry, sandy soils, which usually have an electrical resistivity above 50 ohm-m. Resistivity values of the common types of sandy-clay soils found in the United States range from about 20 to 40 ohm-m. Wet clay soils can have a resistivity of 10 ohm-m or less. (For comparison, the resistivity of sea water is about 0.2 ohm-m.)

The other effect limiting GPR is diffuse scattering caused by small random variations in soil or roadbed properties. This mechanism is particularly important in complicated, layered roadbeds. Radar signal attenuation – and the power restrictions imposed by current FCC rules – limits the effective range of the GPRs to depths of about 2 to 3 m in all but the most dry and uniform soils.

1.2.2 Electromagnetic induction in soil

EM signals in the kilohertz (kHz) range – the induction regime – penetrate through conductive soil by diffusion, not wave propagation. Diffusive signals in soil are subject to a lower intrinsic exponential attenuation rate than propagating radar waves; moreover, this rate can be controlled by adjusting the frequency, with lower frequencies suffering less attenuation. The intrinsic attenuation rate for inductive signals in soil is given by the following approximate formula:

$$\alpha_{inductive} \sim -0.0173 (\sigma f)^{1/2} \text{ dB/m (inductive attenuation rate)}, \quad (6)$$

where $\alpha_{inductive}$ is the attenuation rate in dB/m, σ is the soil's conductivity and f the frequency of the inductive signal. Thus, for example, an inductive signal at 10 kHz in a soil of conductivity 0.02 S/m (resistivity of 50 ohm-m) attenuates at the rate of only -0.24 dB per meter of travel. A 60 dB inductive system could therefore detect signals that have traveled 120 m through the soil (or 60 m down into the earth and back to the surface).

Clamp-on or Direct Field Method

There are two different ways of using inductive signals to map buried utilities. In the direct or "clamp-on" method, electrical current at a specific frequency is injected directly onto a metal pipe from a portable current source by leads connected to the pipe. (To do this, of course, the pipe must be accessible at the surface or below ground, such as in a manhole or beneath a surface valve cover.) The injected currents will tend to flow along the pipe creating a magnetic field that can be detected at the surface. The amplitude of the magnetic field is generally highest directly above the currents. For a steady direct current (zero-frequency) flowing along a long, linear pipe, the strength of the field is inversely proportional to the distance from the pipe:

$$B = 200 I/r \quad (\text{magnetic field in nT}), \quad (7)$$

where B is the magnetic field in nanotesla (nT), I is the strength of the current in amperes (A), and r is the (perpendicular) distance in meters (m) from the point of observation to the pipe (FIGURE C-4 right). In the simple case where the pipe is horizontal and the observation point is directly above the pipe, r is just the pipe's depth, and this formula can be used to estimate the depth to the pipe from the decay of the magnetic field with height above the ground surface.

For frequencies in the inductive regime, there is no simple exact expression (similar to equation 7) for the magnetic field of a long linear current flowing along a pipe in conductive soil. Equation (7) is, however, a reasonable approximation at frequencies less than 100 kHz in soils with conductivity less than about 0.1 S/m at distances less than about 5 m. At large distances (or equivalently with very high conductivities), the decay of the magnetic field is a combination of a geometric factor inversely proportional to the square root of the distance ($r^{-1/2}$) and an exponential decay at the rate given by equation (6). These formulas, along with the sensitivity limits of the detectors and the background magnetic field noise (coming from either natural or other man-made sources), ultimately set the detection limits for the clamp-on method of pipe location.

Indirect or Secondary Field Method

In the indirect or "secondary-field" method, a *primary* EM is generated at or near the surface by driving current through a loop of wire (FIGURE 1 right). As the field of this primary current diffuses into the ground, it generates secondary electrical currents in the soil and in any buried conductive object. The secondary currents generate their own magnetic field, which can be measured at the surface (and in most cases distinguished from the primary field). Software can then process ("invert") these magnetic field measurements to determine the locations of the objects where secondary currents are flowing. It is more difficult to determine the detection limit for the secondary field method, because the amount of current that can be induced on a remote object by induction from the surface depends on many different factors, including the conductivity of the soil, the orientation of the surface loop generating the primary field, and the detailed shape of the remote object.

Nevertheless, because it depends mainly on the channeling of currents by conductive objects, the inductive method is most effective in locating buried metal objects and is much less sensitive than radar to variations in soil conditions. In fact, the ability of induction to detect buried metal objects can actually improve as soil conductivity increases, because any secondary currents flowing in the soil will tend to flow

towards the most conducting objects in the subsurface, which are usually the buried metal utility lines or conduits.

1.2.3 A Mobile Platform for High-Resolution Underground Mapping

Radar and induction systems have been used for many years for detection of subsurface structures, in both commercial and scientific applications. Most “off-the-shelf” commercial units consist of a single sensor pair (one transmitter and one receiver) and are geared for “handheld” surveys in which an individual carries or pulls the unit over the survey area usually making readings at grid laid out in advance. To speed up this process, systems can be mounted on vehicles and combined with GPS to record positions automatically. Even with these improvements, there are limits to the accuracy and efficiency of using individual sensors to survey large areas.

One of the innovations proposed for the Dual Array Project was integration of geophysical sensor arrays into a mobile platform capable of doing high-resolution surveys over large areas efficiently. “High-resolution” and “large areas” are of course relative terms. The resolution and scale targeted for the dual-array system was based on its intended use in the planning, engineering, and inspection of subsurface utility networks, where a resolution and accuracy on the order of inches (centimeters) is needed in locating lines that can extend over miles (kilometers). Achieving these goals would represent a dramatic increase over previous capabilities, and has become possible only within the last few years with the availability of cheap, rugged EM sensors that can be used in multi-channel arrays, with the development of higher capacity data acquisition systems that allow simultaneous recording from many sensors, and with the use of positioning systems that can track the location of sensors accurately enough to allow software to “stitch together” a seamless map from data recorded as the sensor array moves over the survey area.

FIGURE 2 left shows a schematic of such a mobile system. The main components are

- (1) an array of sensors that can record data while in motion,
- (2) a platform (vehicle) for transporting the sensors,
- (3) a positioning system to track the vehicle, and
- (4) software to merge the sensor and positioning data to create subsurface images or maps.

An imaging GPR system with these components was developed by Witten Technologies, in collaboration with Malå Geoscience AB and Schlumberger, in a project partly sponsored by the Electric Power Research Institute (EPRI, www.epri.com) which ran from 1998 to 2000 (FIGURE 3). APPENDIX D briefly describes the imaging GPR system, which Witten Technologies commercialized in 2001 under the brand name *CART Imaging System* (“CART” stands for “computer-assisted radar tomography”).

The major new innovation proposed for the Dual Array Project was the development of an array of electromagnetic induction (EMI) sensors to complement the radar array in the CART system. An important part of this innovation was development of new software that would invert the EMI measurements to obtain the positions of underground pipes and would combine this information with features extracted from radar images to create digital maps of infrastructure.

Two other novel features were proposed for the EMI system. The first was the development and use of compact broadband induction sensors that can record the vector magnetic field simultaneously at a broad range of frequencies from about 50 Hz to 100 kHz. The second was the ability to use the system in either the direct-field inductive method or the secondary-field method. These two modes of operation were called “tracking” and “mapping” modes in the original proposal:

- *Tracking mode* uses one or more “clamp on” transmitters that inject currents at specified frequencies directly onto individual pipes. Use of broadband sensors covering a wide range of frequencies enables

simultaneous tracking of several pipes using currents of different frequencies and allows easier identification and tracking of specific underground lines.

- *Mapping mode* uses a primary magnetic-field source that rides with the sensor array and induces secondary currents everywhere in the subsurface by EM induction. Induced secondary currents will flow preferentially along conductive subsurface objects, which are usually metal pipes or conduits. Mapping mode can give more efficient coverage of large areas (and is the only mode available when there is no direct access to the pipes), but lacks the ability to track individual pipes.

Although the terms “tracking mode” and “mapping mode” are helpful in picturing how the system uses EM signals to detect buried pipes, in both modes the goal of using a broadband sensor array is to map the magnetic field generated by currents induced in the subsurface with enough detail to determine the positions of pipes and thereby create complete underground utility maps. In this report, we will describe the two modes of operating as the direct-field method using “clamp-on” transmitters or the secondary-field method using “on-board” transmitters. These descriptions better capture the practical difference between the two modes of operation.

1.3 Applications of the dual-array system

The primary applications of the technology developed in the Dual Array Project are in pipeline safety and in cost savings during construction. Emphasis on safety in digging and construction has improved dramatically in recent years, with implementation nationwide on the One-Call System, after passage of the Transportation Equity Act of the 21st Century in 1998, and with promotion of the new engineering discipline called subsurface utility engineering (Stevens and Anspach, 1993; Lew, 1996) by federal and state departments of transportation. Despite this, excavation and construction accidents, including accidents during highway construction, remain the chief cause of damage to the nation’s underground networks (see the NTSB Report “Protecting Public Safety through Excavation Damage Prevention,” NTSB/SS-97/01). Comprehensive statistics on utility accidents are difficult to gather, but estimates are that ten of thousands of accidents occur every year, causing damages that amount to hundreds of millions (perhaps even billions) of dollars. For example, information collected by the American Gas Association on major reportable incidents involving gas distribution and transmission pipelines showed yearly damages averaging about \$40M from 1994 through 1999 (see, e.g., Kalisch, 2000). APPENDIX B gives a brief description of the One-Call System (also called “Call Before You Dig”, or “Dig Safely”) and of subsurface utility engineering (“SUE”).

The dual-array system is a prototype of the next generation of geophysical technology for more efficient, comprehensive, and accurate shallow underground mapping. One of the key goals in its development was to produce a system that could create infrastructure maps over large areas in a form that allows their archiving electronically in geographic information systems (GIS). FIGURE 4 shows an example of an integrated map created in GIS from one of the field test surveys.

Although this technology has applications in One-Call Systems, the economics of its introduction to the marketplace (described further in the section 4.2 on “Cost-Benefit Analysis”) will fit better into the mapping activities of SUE, which are intended to save substantial costs during the design and engineering phases of construction. For example, the classic study by Lew (1996), sponsored by the Federal Highway Administration, showed that systematic application of SUE practices could save on average about 5% of the total cost of highway construction projects. This level of cost saving applied to large projects can easily justify the use of advanced new geophysical technology. The dual-array system will also be useful in environmental surveying for leak detection and hazardous waste monitoring.

1.4 Project history and accomplishments

The Dual-Array Project started in October 2002. TABLE 8 in the financial section 5 summarizes the original plan, which called for a project extending over eight quarters with the major milestones as listed. At the end of 2003, WTI requested from USDOT, and was granted, an extension of the project by one quarter. The project finished in December 2004, having met all its major milestones. A final project brief was held on January 12, 2005.

Timeline

The first two quarters of the project were devoted mainly to development and testing of prototype broadband EMI sensors and the data acquisition system. In the first quarter, two prototype “coil pods” built by Electromagnetic Instruments (each consisting of three orthogonal magnetometers) were tested and calibrated. After verifying that these sensors would meet the specifications for the array, designs were made for the full 16 sensor array (48 channels) and for the data acquisition system. The additional sensors were ordered from Electromagnetic Instruments, and two “off-the-shelf” data acquisition systems were tested, resulting in the choice of a commercial system from Yokogawa.

The third and fourth quarters were devoted mainly to assembly of the full 16-sensor array and the data acquisition system and to the design of the platform for carrying the sensors during mobile operation. In addition, in the third quarter we performed the first extensive field tests of the sensors, using two of the coil pods mounted on a small “push cart”. One of the tests was carried out to track pipes behind a group of houses in Cape Cod; the other, to track buried high-power voltage lines forming part of Con Edison’s underground feeder network in the west end of Manhattan. The first year finished with a successful test of the full 16-sensor array mounted on a vehicle. The tests were done over a grid of wires laid out on the ground in a parking lot to simulate buried pipes energized currents at different frequencies.

In the fifth quarter, we made the first field test of the full EMI system, including the sensor platform and positioning system, in a survey conducted in southern Connecticut, for the South Central Connecticut Regional Water Authority. This survey was done in an area that had also been surveyed by the CART radar system, which allowed direct comparison and the radar and EMI results. The southern Connecticut survey also provided the first tests of the full software for merging the data and produced the first large-scale maps of surface magnetic fields created by currents channeled along pipes at different frequencies. Analysis of the recorded magnetic fields showed strong signals at 60 Hz – most likely coming from overhead power lines – which caused the sensors to saturate and rendered parts of the data unusable. To correct this problem, we requested and received an extension of the project by one quarter.

The sixth quarter concentrated on modifications of the magnetic field sensors (to reduce sensitivity to 60 Hz signals) and to the design of an on-board transmitter. These developments were done with Electromagnetic Instruments, which delivered both the modified sensors and the prototype transmitter early in the seventh quarter. In addition, the final modules of the prototype software for handling both clamp-on and on-board transmitters were written and integrated into the software system. The seventh quarter saw the first tests of the modified sensors (a repeat survey of the site in southern Connecticut and the first tests of the on-board transmitter. In addition, a test survey was done for Florida Power and Light (FPL) to test the ability of the sensors to pick up signals injected onto a pipe at a depth of 30 ft.

The eighth quarter was devoted mainly to the final full-scale field test, which was done in collaboration with Con Edison near one of its electrical substations in Elmsford, NY. This surveyed covered approximately 40 000 sq ft in two nights, including tests of both clamp-on and on-board transmitters. In addition, a full survey was done at the same time with a prototype 400 MHz CART system. Activities in the final quarter consisted of analysis of the field test results, which included substantial work on the data processing and inversion software for the on-board transmitter, and writing of the final reports.

2 EMI Array Experimental Prototype

The schematic in FIGURE 2 shows the six main system components of the EMI sensor array.

- (i) Magnetic field sensors,
- (ii) Magnetic field sources,
- (iii) Data acquisition system (DAQ),
- (iv) Positioning system,
- (v) Sensor platform and vehicle,
- (vi) Data processing, interpretation, and mapping software in CAD and GIS.

The experimental prototype or “EXP” built during the project includes all major system components, which were tested extensively in the laboratory and in the field. This section discusses the original specifications, lessons learned during assembly and testing of the EXP, and general areas where the prototype could be improved.

2.1 Magnetic field sensors

The most important component of the EMI array is the magnetic field sensor. Specifications for this sensor determine the overall capabilities of the system – in particular, the depth and size of pipes (or other underground features) that can be detected – and set requirements for other system components such as the magnetic field sources (transmitters), the data acquisition system, the positioning system, and the interpretation software.

2.1.1 Vector magnetometers: 3-axis induction sensors (coil pods)

The sensors used for the EXP are 3-component magnetic field sensors developed by Witten Technologies in collaboration with Electromagnetic Instruments, Inc., a California company that specializes in precision induction sensors. (Electromagnetic Instruments is now a fully owned division of Schlumberger, called EMI Technology Center, www.emiinc.com.) The sensor consists of three induction coils arranged in orthogonal directions and mounted in a 6-inch plastic cube, called a “coil pod” (TABLE 1 and FIGURE 5). The pod also houses integrated pre-amplifiers for each coil. Communication with the sensors is through a single connector, which also includes leads for power supply.

TABLE 1. EMI SENSOR SPECIFICATIONS

<p>Side length: 6 inches (15 cm)</p> <p>Weight: 8 lbs (3.5 kg)</p> <p>Noise levels: 0.0005 nT @ 1kHz 0.0001 nT @ 10kHz</p> <p>Bandwidth: Flat from 500 Hz to 50 kHz Approx. linear fall-off outside band</p> <p>Analog output: +/- 10V</p> <p>Sensitivity: 120 mV/nT</p> <p>Power: +/- 12V</p>	
--	--

The induction coils, which were specially designed for the project using “current-feedback” technology developed and patented by Electromagnetic Instruments (Conti, 1992), are unique for their combination of extremely high sensitivity and broad frequency response. For example, the minimum detectable signal above the intrinsic sensor noise level in the kHz range is about 10^{-4} nT (10^{-13} T), which corresponds to the magnetic field at a distance of 2000 m generated by a current of 1 mA (10^{-3} A) flowing along a pipe. The noise level is about a factor of 10 below the natural background magnetic fields in the kHz range, which set the ultimate limit on the detectability of man-made fields. (The natural magnetic fields at frequencies above about 1 Hz are caused by lightning discharges, which excite electromagnetic wave that propagate around the world in the region between the earth’s surface and the ionosphere.)

We calibrated the coils in the first two sensors by inserting the coil pods into a long solenoid (168 in. long with a diameter of 12.75 in). The tests showed that all six induction coils (3 sensors each in 2 pods) had nearly identical response curves over the entire range of frequencies tested (FIGURE 5 bottom). The original coils had an essentially flat frequency response over the range from about 100 Hz to 100 kHz, with the response falling off linearly outside this range. To prevent aliasing when the signals are digitized, an analog low-pass filter in the pre-amplifier cuts off the frequency response at the upper end at about 1 MHz. No high-pass filter was used for the original sensors, and their response was significant (about 30 dB down from the peak) at frequencies as low as 10 Hz. As described below (section 3.4), the first large scale survey with the EMI array registered strong 60 Hz fields coming from local power lines, which were strong enough to saturate the receivers at normal gain settings and render large portions of the data unusable. The sensors were therefore modified to include an analog high-pass filter in the pre-amplifier to increase the roll-off in response at the lower frequencies (FIGURE 6). Even with this modification, the sensors can still easily record 60 Hz fields coming from buried or overhead power lines, but the 60 Hz fields no longer dominate the fields at other frequencies.

2.2 Magnetic field sources

This section briefly describes the magnetic field sources (“transmitters”) developed for the EMI sensor array. As described in the overview, the array was designed to operate using either clamp-on transmitters that attach directly to pipes or on-board transmitters that induce currents remotely in the soil. Both types of sources are commercially available. Tests showed that commercial clamp-on transmitters worked well with the array, but no off-the-shelf induction transmitter was available that could work effectively at the range of frequencies covered by the sensors. To complete the system, a new induction transmitter was developed with Electromagnetic Instruments.

2.2.1 Clamp-on Transmitter (current injection source)

Clamp-on sources operating at several discrete frequencies are available at low cost with many different commercial systems used for utility locating. Three of the most popular brands are

- Radiodetection (www.radiodetection.com)
- MetroTech (www.metrotech.com)
- Subsite Electronics (www.ditchwitch.com)

Tests of representative systems showed that they were generally suitable for use with the EMI sensors, having an adequate range of frequencies, sufficient power, and enough battery life even for large-scale field tests. We purchased two units (model T10) from Radiodetection, priced at about \$2.5k each. In addition, Witten Technologies owned another Radiodetection unit (model RD433HCTX-2), which was also used during the project. The top of FIGURE 7 shows pictures of the units.

Clamp-on sources use both galvanic and toroidal clamps for injecting currents onto pipes. A galvanic clamp has two metal leads: one is placed in direct contact with a metal surface of the pipe, creating a

direct path for current to flow from the source onto the pipe. The other lead is normally attached to a stake grounded in the soil, but in principle could also be attached to another point on the pipe (preferably at a distant location) to complete the circuit. A toroidal clamp creates currents on the pipe inductively with a magnetic circuit that encloses the pipe, generating a time-varying magnetic field that circulates around the pipe. Toroidal clamps must operate at a finite frequency and can only generate (appreciable) currents along the pipe if it is in contact with conductive soil at some nearby location. An advantage of toroidal clamps is that they can be used when the accessible surface of the pipe is coated with insulating material. Generally, galvanic clamps work best under most conditions, but do require contact with a clean metal surface of the pipe.

2.2.2 On-board Transmitter (induction source)

Some commercial transmitters for utility locating (e.g., units from Radiodetection or MetroTech) can also operate by remote induction, by driving current through a small loop inside the transmitter that is tuned to a specific frequency. The loop acts as a portable magnetic dipole source and will induce secondary currents in the soil, whose magnetic field can be picked up by unit's tuned receiver coils.

Tests of the Radiodetection source and discussions with other manufacturers indicated that none of transmitters available "off-the-shelf" could operate effectively over the broad range of frequencies covered by the sensors in the EMI array. We therefore decided early in 2004 to work with Electromagnetic Instruments to design and build a new transmitter for this project.

The initial specifications were as follows:

- Coils transmitting along 3 orthogonal axes, with independent ON/OFF switches.
- Frequency range from 500 Hz to 50 kHz, adjustable in frequency steps of at least 1 kHz. This range and fine adjustment gives maximum flexibility in avoiding local frequency interference, VLF frequencies or strong site-specific background noise. The exact actual frequencies of transmission are usually not important, except for special frequencies where ambient noise is large (e.g., at harmonics of 60 Hz).
- Moment of 5 at 1 kHz to provide ample induction power. Design of the transmitter loops should allow for adding or subtracting of turns to adjust the moment as necessary. It turned out that for no additional cost a 5-stage gain switch (0, 25, 50, 75, and 100%) was included for each transmitter loop.
- Electronics packaged in a separate waterproof (Pelican) box with outputs of one reference signal for each of the three transmitter signals and one combined transmitter reference signal (all through a BNC connector). The combined transmitter reference signal should be the result of three passive current monitors in series. Those output signals will be used as references for the received signals. It turned out that a single pick-up coil mounted in the center of the three coils wrapped around the center pole (FIGURE 7 bottom), oriented so that it can receive partial signal from each loop was able to provide the needed reference signal.
- DC power supply +/-12V, compatible with existing power sources in the system.

We expected that these specifications could be met with a 3-coil transmitter that would fit into a 0.5 m cube and could be mounted on a rigid boom between 6 and 10 feet behind the receiver array. A fixed geometry between the transmitters and receivers is important for accurate remote induction measurements, since variations in the distance or orientation between the transmitter and receiver coils will change the primary field (the direct coupling between the transmitter and receiver through air), making it difficult to estimate the smaller secondary field coming from subsurface currents.

The bottom of FIGURE 7 shows a picture of the transmitter developed by Electromagnetic Instruments. Each of the three circular PVC tubes carries a transmitter loop of 0.7 m diameter. The two thick tubes inside the sphere provide support to mount the sphere behind the receiver array. The diameter of the

transmitter coils was increased to 0.7 m (from 0.5 m in the original specifications) to increase the transmitter moment while reducing the power requirements of the transmitter driver electronics (the moment of the coils is proportional to the current times the area of the loop, which of course increases as the square of the coil diameter).

The three loops are arranged with their axes pointing along orthogonal directions. The overall configuration of the coils allows two different mounting options that either maximize or minimize the direct coupling between the transmitter and the receivers. Maximum coupling between the transmitter and receivers occurs when the planes of the three transmitter coils are aligned parallel to the planes of the 3 coils in the magnetic field sensors (equivalently, when the dipole moments of 3 transmitter coils are aligned respectively with dipole moments of the 3 receiver coils in each coil pod). In this orientation, the direct (free-space) coupling of transmitter and receiver is a maximum when all three coils transmit at the same field strength and the outputs of three receiver coils (in any coil pod) are added coherently. Under these same transmitting and receiving conditions, there is also an orientation of minimum (in principle, zero) coupling that can be obtained by rotating the transmitter coil so that the vector sum of the transmitter dipole moments is orthogonal to the vector sum of the receivers' dipole moments.

Theoretically, the results of transmitting in the two different orientations (and in any other orientation) can be synthesized by transmitting independently from each coil, recording the outputs at the receivers and forming vector sums of the data. Different orientations can, however, exhibit practical differences, if the direct coupling is strong enough to saturate the response of the receiver coil. In any case, information about the pipes is in the secondary magnetic field – i.e., in the magnetic field created by secondary currents induced in the pipe by the primary field of the transmitter. This secondary field has a different phase than the primary magnetic field and, with an accurate time reference between the transmitter and receiver coils, can usually be extracted accurately with signal processing.

The total weight of the transmitter sphere is estimated at about 14 lbs (6.5 kg). A boom made of lightweight carbon fiber tubes, with high torsional stiffness and strength, was built to hold the transmitter behind the receiver array.

The new on-board transmitter cost about \$29k to develop with Electromagnetic Instruments. We estimate that additional transmitters will cost around \$7k each to produce.

Full use of on-board transmitter requires estimation of the phase shift between the transmitter and receiver signals. To allow this, the data acquisition software needs to record a reference signal from the transmitter needed that can be correlated with the magnetic fields measured by the sensors to extract signals in-phase and out-of-phase with the primary signals. The on-board transmitter has one combined reference signal only for all three transmitter loops, which requires that one channel of the data acquisition system be used to record the transmitter reference signal. The combined reference signal is split into its three transmitting signals during data processing of on-board data.

2.3 Data acquisition system

After the magnetic field sensors, the next most important component of the EMI system is the data acquisition (DAQ) system, which samples and digitizes the analog signals from the sensors and transfers the bits to the acquisition computer for storage. To speed up development and testing of the prototype, we decided to use a commercial DAQ system purchased “off the shelf”. This section describes briefly the requirements and specifications for this unit, our tests of the commercial systems in the lab, and the choice of system for the EXP. In fact, only two manufacturers produced commercial systems capable of meeting the specifications within the budget: IOtech (www.iotech.com) and the Yokogawa (www.yokogawa.com). We tested systems from each of these manufacturers, as described briefly below, and chose a system from Yokogawa. Quarterly Report 2 contains further details of the tests.

2.3.1 Requirements and specifications

The DAQ system must digitize and record a time-series for each of the sensors – 48 separate channels in the EXP, corresponding to 3 coils in each of 16 coil pods – with enough resolution to cover the dynamic range of the sensors over their full bandwidth. The system also has to operate fast enough to allow street surveying with a slow moving vehicle and has to be rugged enough to work on a flatbed trailer.

The precise specifications are determined as follows.

- *Sampling rate.* Most commercial transmitters provide signals at one frequency just below 10 kHz, one between 30 and 40 kHz, and one or more frequencies above 40 kHz. For the example, the Radiodetection T10 provides signals at 8.2, 32.8, 65.5, 83, and 200 kHz. We decided to set 500 kHz as the upper limit for frequency which implies a Nyquist sampling rate of 1 MHz to avoid aliasing.
- *Dynamic range.* The analog range of the induction coil sensors requires 14 bit analog-to-digital conversion. This figure is obtained by equating the noise level of the sensors to the field level that would be represented by the lowest-order digital bit. Let ADC_BITS be the number of bits for analog-to-digital conversion. If the lowest-order bit is equal to the *Noise Level* of the sensors, then the total digital signal range represented is $2^{ADC_BITS} * Noise\ Level$, which should be equal to the analog signal range at the highest gain setting for recording; that is,

$$2^{ADC_BITS} * Noise\ Level\ (nT) = Analog\ Range\ (mV) / Sensitivity\ (mV/nT),\ or$$

$$ADC_BITS = \log_2 (Analog\ Range/Sensitivity/Noise\ Level).$$

The highest resolution analog range available with the acquisition system is 400 mV (+/- 200 mV at the highest gain setting). Using the noise level of 0.0001 nT (at 10 kHz) then gives 14 bits needed to cover the full range of signals that can be recorded by the sensors using the digital acquisition system.

- *Data transfer rate.* The most demanding requirements are on the data transfer rate; i.e., the rate at which (digitized) data can be written to disk. This rate is set by the following factors:

Channels: 48

Sampling Rate (samples/s): 1 MHz (10^6 samples/s) for each channel

ADC_BITS (bits/channel): 14

Recording Time (s) needed for an accurate spectral estimate: ADJUSTABLE

Spatial Sampling (ft): ADJUSTABLE

Vehicle Speed (ft/s): ADJUSTABLE

The key adjustable parameters that determine the required transfer rate are the *Recording Time*, *Spatial Sampling*, and *Vehicle Speed*. The *Recording Time* is determined by the number of cycles needed to get an accurate spectral estimate at the lowest frequency to be measured. For example, if 1 kHz (1 cycle per ms) is the lowest frequency to be measured, and the signal must be averaged over 4 cycles to estimate the spectrum accurately, then the recording time must be at least 4 ms. The *Spatial Sampling* interval depends on the expected spatial variation of the fields. In most cases, an sampling interval of 1 ft should be adequate. These two factors determine the total number of bits recorded per ft as follows

$$Bits/ft = Channels * Sampling\ Rate * ADC_BITS * Recording\ Time / Spatial\ Sampling$$

Using the numbers above gives

$$Bits/ft = 2.7 * 10^6\ bits/ft\ or\ 2.7\ Mb/ft$$

The maximum speed of the vehicle then determines the required transfer rate according to

$$\text{Transfer Rate (Bps)} = \text{Bits/ft} * \text{Vehicle Speed (ft/s)}.$$

For example, using a speed of 30 ft/s (about 20 m/hr) and the other numbers gives

$$\text{Transfer Rate} = 80 \text{ Mbps}$$

As discussed below, this is within the range of commercial off-the-shelf DAQ systems.

Real-time

It is interesting to compare the data transfer computed above with rate required for true “real time” recording, in which the data would be digitized and stored to disk as fast as it can be collected by the sensors. This rate is simply the product of the number of channels, the sampling rate per channel, and the ADC resolution (bits per sample):

$$\text{Real-time Transfer Rate (Bps)} = \text{Channels} * \text{Sampling Rate} * \text{ADC_BITS}$$

An array of 48 channels sampled at the 1 MHz and 14 bits/sample requires data transfer to storage of 670 Mbps. This is beyond the range of current “off-the-shelf” DAQ systems, but should be achievable within a few years. With real time recording, the only limitation is the speed of the vehicle would be the recording interval (total recording time) needed to achieve adequate spectral estimation of the lowest frequency signal.

2.3.2 Comparison of DAQ systems

A survey of commercial DAQ systems turned up only two off-the-shelf units that were close the meeting the full specifications: the Wavebook 516 from IOtech (www.iotech.com) and the WE7000 system (using multiple WE7275 modules) from Yokogawa (www.yokogawa.com). TABLE 2 compares the key specifications of these systems.

TABLE 2.	IOtech Wavebook 516	Yokogawa WE7000
ADC Resolution	16 bit	14 bit
Capacity	288 channels, in groups of 8	48 channels
Sampling rate	up to 1 MHz	up to 1 MHz
Data transfer	500 kbps Enhanced Capability Parallel Port at time of purchase Now available a 100 Mbps Ethernet	100 Mbps Ethernet
Minimum sample length	none	5 ms
Latency	1 s between channels unless add-on sample-and-hold module is used	Simultaneous
Built-in Filters	Low-pass filter at 200 kHz built-in tunable filter module optional	Anti-aliasing filters tunable from 20 Hz to 40 kHz
Power	AC or DC	110 V AC
Cost	\$6k for 8-channels	\$56k TOTAL for 48 channels

The IOtech and Yokogawa systems are virtually identical in terms of their abilities to record a single magnetic field time series from the sensors. For example, FIGURE 8 (bottom left) compares the ambient fields in the office as recorded by the systems with a sampling frequency of 1 MHz. (This experiment was performed with a demonstration model of the WE7000.) The peaks in the spectra represent strong

background magnetic fields (coming from unknown sources). Except for a minor frequency shift, the two systems produced identical results. The shift, which is likely caused by the IOtech software, would not affect the ability of the system to locate pipes, because only the variation of the peak value with respect to position is used in the inversion scheme that determines the pipe locations.

The main specification that favors the Yokogawa system is the data transfer rate, which determines the speed at which multiple channels can be digitized and recorded. We tested the Wavebook model 516 with an Enhanced Capability Parallel Port for data transfer, which allowed a data transfer of about 0.5 MHz used by all channels. But this setup could not be extended easily to cover all 48 channels for the full sensor array. The Wavebook system can actually accommodate up to 288 channels, but each group of 8 channels must be packaged into a portable box with a common data transfer link to the controlling computer. If the 8 channels are digitized at 1 MHz, they have to share the data transfer link sequentially, which would slow data acquisition speed to much less than 1 mph. If the 8 channels share the parallel port transfer link simultaneously, the maximum digitization rate per channel would be 62.5 kHz for the acquisition to keep up with the transfer. This corresponds to a maximum recordable signal frequency (without aliasing) of only 31.25 kHz, which is not sufficient to cover the full bandwidth of commercial clamp-on transmitters. (The new model 516E uses an Ethernet connection at 100 MHz, so that this is no longer a limitation of the IOtech Wavebook.)

The 100 MHz Ethernet bus of the Yokogawa system allows 1 MHz sampling of all 48 channels at a data acquisition speed up to about 25 mph (using the example of the previous section). This acquisition is more than adequate for the EXP and probably sufficient for a fully commercial system. In practice, we discovered that overhead from the data acquisition software limited the effective speed to about 20 to 30 Mbps. This reduced the maximum speed for data acquisition to less than 5 mph for the EXP and is one of the areas to be improved with the full system.

The AC power requirement of the Yokogawa system was a concern, because a moving AC power supply may create interference with the EMI sensors. Tests showed that this interference could be reduced to an acceptable level by placement and shielding of the generator on the sensor platform (see Quarterly Reports 3 and 6).

2.4 Positioning system

A positioning system is needed to measure and record the location of the sensor array as it moves along the ground mapping the magnetic field. The accuracy of the positioning system is determined by final accuracy needed in locating features in the final underground maps. The speed is determined by the need to create a complete map of the field over a large area in a reasonable amount of time. This is done by "stitching together" swaths of data recorded as the system moves over the area to be surveyed (FIGURE 9). The width of the each swath is essentially the width of the sensor array; the shape depends on the path of the vehicle and can be very complex, since the vehicle is often moving in traffic or around obstacles.

For the dual-array EXP, we decided to employ the positioning method used by the CART Imaging System (Burns et al., 2004). This method solves the problem of merging data collected along complex survey paths by using two complementary systems: (1) a surveying instrument that measures the position of the sensor array very accurately at frequent intervals along its path and (2) a survey wheel that triggers data collection by the array at fixed distances along the path (for a different approach, see Lehmann and Green, 1999). The main advantage of this combined method is that it allows the surveying instrument and sensor array to operate independently. Moreover, by using modern laser surveying instruments to measure position, the method can achieve an accuracy of a cm or less in determining the positions of an array moving at speeds up to about 10 to 15 miles per hour. This capability is still beyond the specifications of systems that use GPS for positioning. Accuracy in positioning at the cm level is needed

for high-resolution synthetic-aperture GPR imaging and is also needed to achieve the highest quality standards in SUE (Anspach, 1995).

The CART positioning system works as follows:

- (1) Data collection proceeds with a series of “profiles”, which are paths of the vehicle covering the area to be surveyed. Each profile contains frames of data, which are the simultaneous (or nearly simultaneous) recordings from all sensors when the array is at a particular position. (All channels are recorded for 5 ms simultaneously within 1 μ s with the EM system, which can be considered “instantaneous” given that the speed of the vehicle is generally less than 1 m/s.)
- (2) The starting and ending points of each profile are first measured accurately with the surveying instrument while the system is stationary. The system then starts to move along the profile with the survey wheel set to trigger a frame of data acquisition at set intervals along the profile path. With the radar unit, this interval is typically every 10 cm; with the EMI unit, 30 cm is usually sufficient. The surveying instrument is also set to record the precise position of the sensor array at pre-set intervals along the path. The intervals for position measurements are typically larger, from 100 or 200 cm.
- (3) To calculate the position of each recorded channel in a profile, software performs the following steps:
 - (a) A continuous path interpolating the position of the reflecting prism along the profile is computed by fitting a cubic spline through its sampled (3D) positions measured by the total station.
 - (b) The path of the survey wheel is computed by applying a (measured) spatial offset to the prism path, and this path is populated with evenly spaced points corresponding to the frame intervals.
 - (c) The position of each channel in a frame is computed by applying its (measured) offset from the survey wheel path.

Birken et al. (2004) give details of the algorithms for computing the (3D) profile paths of the vehicle from the measurement of the laser surveying system, for distributing the array data properly over the swath covered by the array, and for interpolating the data onto a regular grid (if necessary for further processing).

Position measuring system

The positioning method described above requires a system for measuring positions accurately respect to a fixed reference point. The CART system uses a surveying instrument called a laser theodolite (or total station) to measure the position of the array. Laser theodolites measure position by recording the time-of-flight and the directional angles of a short infrared laser pulse sent between a base station and a reflecting prism mounted on the object to be tracked (FIGURE 10). Modern laser theodolites can measure positions with an accuracy of about $\pm(1 \text{ mm} + 1 \text{ ppm})$, which is equivalent to an accuracy of 2 mm over a distance of a kilometer. Angle measurements are accurate to about 1 arc-second. The systems typically have a range of 1 to 2 km. This level of accuracy is probably higher than necessary for the EMI system alone, but is needed for creating high-resolution synthetic-aperture GPR images (Birken et al., 2002). In addition, underground mapping applications such as subsurface utility engineering require accuracies of a cm or less in locating existing pipelines and conduits for planning new construction.

Another important practical reason for using a total station is that it helps with the creation and use of the final underground utility maps. By using the total station to record the position of surface features – such as curb lines, manhole or valve covers – in the same local coordinate system used for the radar and EM data, it is easy to create a final map in which all underground features are referenced to local surface features. The maps can also be referenced to global coordinates by measuring the position of the base station or any other known station within the local coordinate system with an accurate GPS system.

The total station used for the CART and EMI array is equivalent to the Trimble 5600 Series (<http://www.trimble.com/5600.html>). The total station in the CART system is operated in a self-tracking mode in which the base station is programmed to monitor the position of the reflecting prism quasi-continuously with a stream of pulses and then to trigger an accurate measurement – by averaging over many pulses – after a certain elapsed distance. In the Trimble 5600m, the tracking measurements can be made every 0.4 s; the accurate measurement requires about 3.5 s. The positioning software includes algorithms to correct for the motion of the vehicle during the accurate measurement.

Discussion

The positioning method for the mobile sensor platform described above assumes that the relative positions of prism, survey wheel, and array remain fixed during data acquisition, which is reasonable if the system is rigidly assembled. The method also assumes that the unit stays on a level surface and does not rotate around the axis defined by the measuring pole as it moves along the ground. In fact, determining the absolute position of the sensor array in space (assuming that it is a rigid object) requires 6 separate measurements: a measurement of the 3D position of a fixed reference point on the array, and 3 angles (such as the Euler angles) to determine its orientation in space. One improvement planned for ENP would be to supplement the positioning system with on-board tilt sensors that would allow a full reconstruction of the 3D position of all array elements.

2.5 Sensor Platform and Vehicle

The platform for the EMI sensors in the EXP is shown in FIGURE 11. Its main components are the sensor “bookcase” and trailer frame. The “bookcase” holds the coil pods in the array configuration and rides on the trailer frame which connects to the towing vehicle. The platform should contain as little metal as possible to reduce interference with the EM measurements. We designed the platform working with Fenrir Industries out of Stamford (CT), a company that has experience in building non-metallic trailers. Fenrir built the trailer frame for the EXP using a special material called Extren fiberglass. The axle, tongue, and wheels are attached to the frame and are the only metal parts of the trailer itself.

The sensor bookcase, mounted on the frame, is 8 feet wide and contains 90 slots (6 rows and 15 columns) allowing arrangement of the sensors in different array configurations. The bookcase is fitted with a lid that can be closed to protect the sensors during surveys. The cable providing power and communication with the sensors passes through openings on the back side.

The three pictures on the top right of FIGURE 11 show how the cables, which provide the power to the coil pods and send the magnetic field signals back to the splitter box are connected and routed. The power and signal splitter box is located inside the main compartment of the trailer. The box is powered with a custom rechargeable battery supply (gray box left of black splitter box). The signal outputs from the splitter box are routed through three openings in the front wall of the main compartment to the DAQ system compartment.

The mounting of the bookcase allows different configurations for surveying and for transportation. For surveying, the bookcase sits behind the main equipment compartment with its long axis perpendicular to the direction of travel, for transportation, the bookcase sits on the side of the main equipment compartment to reduce the profile of the trailer (FIGURE 11 top left).

2.6 Software

The software processing chain for the EMI array consists of 5 steps

- *Acquisition.* The acquisition software controls the DAQ board, sets adjustable data acquisition parameters for triggering the sensors, and handles communications between the DAQ, other electronic components and the acquisition computer where data are stored.

- *Pre-processing*. The pre-processing software extracts the magnetic field time series for each sensor, applies whatever digital filters are necessary to clean up the signals and extracts a frequency spectrum, which includes the amplitudes of the magnetic fields at the frequencies of the transmitter currents.
- *Positioning and Geometry*. The geometry software extracts the positioning information from the data files recorded by the laser theodolite, calculates positions of the sensors for each frame, and sets up the 3D data structures needed for inversion and mapping.
- *Inversion*. The inversion software solves an optimization problem to estimate the positions of a network of underground pipes, with currents flowing along each pipe that generate a surface magnetic field that best matches the data.
- *Mapping*. The mapping software takes the inverted positions of the pipes and the surface features mapped during data acquisition and converts these into data structures that can be read by standard mapping software, e.g. CAD or GIS, where the final maps are composed.

The sections below briefly describe each of these steps.

2.6.1 Acquisition Software

FIGURE 12 (left) shows the virtual control panel of the software module that controls the data acquisition for the EMI array typically ran on a laptop field computer. This interface was written in LabVIEW (www.labview.com) mainly to provide a flexible graphical user interface (GUI) for field testing the prototype. FIGURE 12 (right) shows visualizations of the data from several different software modules. Those modules have been created in the LabVIEW and MATLAB programming environments and are used for exploring various aspects of the data and to assess the data quality. Individual time series and their corresponding frequency domain equivalent can be plotted in various ways.

The acquisition software includes functions for controlling the different electronic hardware components (sensors, DAQ, trigger wheel); for monitoring the data acquisition (e.g., displaying the speed of the vehicle); for plotting and manipulating data in the field.

The interface allows control of the following main settings:

- Initialize, test, configure and control all electronic hardware components of the system:
 - DAQ boards
 - Serial port communication
 - Survey wheel counter electronics
 - Calibration of survey wheel
- Manage survey specific geometry and general information:
 - Track of the locations of the coil pods in the sensor shelf
 - Keep track of the positioning system prism pole location
 - Assign channels to individual sensors
 - Manage the transmitter information
 - Manage miscellaneous project information such as operators, location, date, time, etc.
- Control data acquisition settings:

- Configure DAQ channel settings, such as number of time samples, sampling frequency, gain, filter, etc.
- Set one of the following four trigger modes for data acquisition:
 - Single manual trigger
 - Time trigger (i.e., every N seconds)
 - Distance trigger with software command
 - Distance trigger with hardware command (from counter wheel)
- Acquire data depending on settings above:
 - Control the triggering of the data acquisition and acquires a frame of data with each trigger (A “frame” of data is the recording over a fixed time interval of a time series simultaneously from each channel of the array.)
 - Download the acquired data from the DAQ stations
 - Store the data in binary data files and a matching text header file containing the description of the data file, the time and survey wheel distance of each trigger and all other hardware acquisition settings
 - Display the acquired data

2.6.2 Preprocessing Software

Preprocessing software consists mainly of routines for reading in the raw time magnetic field series stored in “profiles” during data acquisition, checking that data was recorded consistently from all sensors (and flagging bad sections of data, if necessary), and finally computing a spectrum to extract the magnetic field amplitudes at the frequencies of interest. The most important step of course is extracting the spectrum. Normally, the digital time series are recorded with a fine-enough sampling interval and for a long-enough period to allow use of the Fast Fourier Transform to compute the spectrum. (More sophisticated routines, which involve fitting the time series to a discrete set of selected frequencies, were also developed to handle noisy and clipped data. See Quarterly Report 4.) A Gaussian window function is used to reduce end effects for short time series. The top right plot of FIGURE 12 shows a sample time series from one sensor and the corresponding spectrum. In this example, two transmitters were broadcasting: one at 8.2 kHz and the other operating at 32.7 kHz. The spectrum of the output signal has peaks at the two transmitted frequencies.

FIGURE 12 also shows a different display used for quality control. In this plot, the spectrum computed from a single sensor at different times (usually corresponding to different positions of the array) is displayed as a contour plot with color indicating different spectral levels (red are high values; blue, low). The large band of red at the left corresponds to magnetic field noise from 60 Hz power lines, while the high-amplitude spectral components at multiples of 20 kHz correspond to noise from the AC power generator used for the DAQ system. The lines at about 8 kHz and 32 kHz correspond to transmitter frequencies used for this survey.

2.6.3 Positioning and Geometry Software

The software to handle positioning for the CART system is well suited for the EMI array, but required some small modifications since the geometry of the sensors in the EMI array is more complicated than that of the radar antennas in the CART system. The radar has only 16 separate “sensor channels” (source-receiver combinations), and all sensors are aligned in the same direction and are at the same height above ground (when the unit is on a flat surface). The EMI array has 48 separate sensor channels,

with each channel in one of 3 different orientations. In addition, individual channels of EMI array can be at six different heights.

We use the following data structure, implemented in MATLAB, to keep track of the EMI array geometry:

- (1) A local Cartesian (x,y,z) coordinate system is defined with respect to the array (which is assumed to remain rigid at all times). Definition of the coordinate system includes the location of the origin and the direction of the axes with respect to the array elements. Typically, the origin is chosen to be the center point of the array; the x -axis is parallel to the array; the y -axis is the direction of travel, and the z -axis is upwards. (The direction of the x -axis is chosen to form a right-handed coordinate system.)
- (2) The position of the reflecting mirror of the prism is recorded in the local coordinate system.
- (3) The position of the center point of each receiver coil is recorded in the local coordinate system.
- (4) The orientation of each coil is recorded with respect to the axes of the local coordinate system.

This information is sufficient, when combined with the output of the laser positioning system, to compute the global position and orientation of each receiver coil using the positioning method described above.

2.6.4 Inversion Software

The output of the pre-processing and positioning software is a series of magnetic field maps over the survey area, showing different components of the magnetic field at selected frequencies. On the right of FIGURE 15 an example map from one of the first larger field tests of the system is shown (section 3.3). Strong linear features in these field maps correspond to narrow highs (or lows) of the field amplitude and provide a good qualitative guide to the locations of buried lines. (The horizontal magnetic peaks directly above a linear current filament; the vertical field is null.) To obtain quantitative results, inversion software was developed to solve for the locations of a network of current filaments (representing currents flowing along the buried lines) whose magnetic field best matches the surface measurements. A starting model, consisting of a number of current filaments and their possible intersections, is input to the program, which iteratively adjusts the horizontal and vertical positions of the endpoints of each filament, and also the amplitude of current flowing along each filament, to match the surface measurements. The software can use either a 1D or a 3D inversion algorithm. The 3D algorithm adjusts both the horizontal (x,y) and vertical (z) positions of current filaments and allows the current amplitude to vary linearly along the filament (to represent current leaking into the soil). In addition, the 3D inversion algorithm can handle a starting model in which current filaments intersect (representing connections between buried lines) and will conserve current flow at the junctions. The 1D algorithm works on profiles of data and adjusts only the lateral positions and depths of pipes in a cross section. Examples of the output of the two different algorithms are given below in discussion of the field tests.

APPENDIX E provides a full description of the mathematical model and algorithms used to solve the inversion problem.

2.6.5 Mapping Software and GIS

The mapping software includes routines for conversion of pipe locations determined from analysis of EMI data and radar images into CAD and GIS. The software for conversion to CAD is currently in the form of AutoCAD scripts that import data from the data analysis package (in MATLAB) into AutoCAD. (There is also an AutoCAD script for conversion of CAD to Microstation format.) Information imported includes geometry information recorded at the time of surveying (profile paths, mapped surface features) and 3D locations of pipes. Client engineering drawings (in CAD format) or scanned maps can also be imported for overlays. Production of a final map in CAD is usually sufficient for most engineering applications.

An optional step is to record the results in absolute geographical coordinates; for example, in a mapping database provided by a geographical information system (GIS). Software was developed during the project for converting between CAD, which is still the standard for engineering drawings, and GIS. The conversion process, undertaken using AutoCAD Map and ArcGIS has the following components:

- Translate local coordinates of AutoCAD project to global coordinates (if not already assigned in the field). Manual translation requires a control map in the required coordinate system (usually, a high-resolution orthophoto).
- For radar data - set background transparency, and merge individual radar images into one seamless image for each depth slice. Export depth slice images with accompanying correlation file (tiff world file - *.tfw).
- Convert points, polygons and lines by exporting each feature class separately to a shape file. Feature depth is maintained by exporting polylines as individual line segments with associated z attribute data for the start and end points of the line.
- Custom symbols have been developed in ArcView to match the CAD symbols. Feature symbols are automatically assigned for standard themes (e.g. WTI_PIPES_1), or can be matched by attribute for non-standard features.

FIGURES 4 and 37 show composite GIS maps created with these software components. The map in FIGURE 4 includes a depth slice through the radar image, EM data, and interpreted pipe locations, all superimposed on a high-resolution aerial photograph.

3 Field Tests

This section summarizes the main field tests of the sensors and the array, which are listed in TABLE 3. The sensor tests were intended either to check performance of the individual sensors in realistic settings, or to test capabilities of the data acquisition or processing systems. The array tests were carried out with the fully assembled system, including the trailer. Three of the tests used the full positioning system and were carried out at locations where the CART radar system was also used, providing a simulation of the full dual-array system.

TABLE 3. Field Test Summary

Sensor field test	Apr 2003	Sandwich, MA	First sensor and software test
	May 2003	Manhattan, NY	Con Edison, oil-o-static
	May 2004	Jacksonville, FL	FPL, deep pipe
Array field test	Sep 2003	Newton, MA	Mock-up system test
	Nov 2003	Southern	RWA, full system test with positioning, 200 MHz radar
	Apr 2004	Connecticut	
	Jul 2004	Manhattan, NY	Con Edison, oil-o-static
	Jul 2004	Elmsford, NY	Con Edison, substation, full system test with positioning, clamp-on and remote transmitter, 400 MHz radar

3.1 Sensor Tests: Apr 2003 Cape Cod

In April 2003, we surveyed approximate 2500 sq ft of a grassy area between summer cottages in Sandwich, Cape Cod. This was the first test of the sensors and software in a realistic survey to track currents injected onto buried pipes with a clamp-on transmitter. FIGURE 13 shows part of the surveyed area, including the location where the inductive clamp was used to inject currents at 32.8 kHz onto an electrical line where it emerges from the ground.

The survey was carried out with 2 coil pods mounted at two different heights on a small “push-cart”. The plots at the bottom of FIGURE 13 show the magnitude of the horizontal magnetic field recorded (by the lower sensor) over the area surveyed. Readings were made on a grid with spacing of 1 ft between successive readings along each profile (y direction) and spacing of 2 ft between successive profiles (x direction in the plot).

The magnetic field contours suggests that several electrical cables emerge from the back of the houses, and then follow a single path towards the right end of the survey. An initial guess containing three pipes was constructed based on this magnetic field plot. The inversion produced the pipe locations indicated by the green lines, with all node points between one and two feet below the surface. This estimate of the locations of the pipes is consistent with the layout of the electrical grid that supplies power to the cottages at the survey site.

3.2 Sensor Tests: May 2003 Con Edison West End Avenue and 59th Street

In May 2003, we conducted a survey for Con Edison to track high-voltage power lines along West End Avenue near 59th Street. FIGURE 14 shows the configuration of the lines, which are part of the buried feeder network that supplies power to Manhattan. The exposed trench contains 4 conduits: two 10-in.

diameter metal conduits carry oil-coiled power lines and two 5-in. diameter conduits carry only oil to complete a loop for circulating the coolant. (These high-voltage lines are called “oil-o-static” for historical reasons related to the original manufacturer of the coolant system.) An important application of the EMI system for Con Edison is to determine the locations of the individual pipes in the trench, which often deviate from the standard configuration in order to avoid obstacles, such as crossing pipes. To complicate this problem, oil-o-static trenches are often covered by steel plates to protect the lines where they are close to the surface.

The purpose of the survey was to verify that it would be possible for the sensors to pick up signals from currents injected onto individual pipes in the trench and to estimate the distance from the injection point at which currents injected along the pipe could be tracked. We tested injecting currents with both toroidal and galvanic clamps. The toroidal coupling was not very effective, because of a mismatch between the size of the pipes and toroidal rings available and also (we believe) because the pipes were insulated for a long distance so that there was no ground return loop for the secondary inductive circuit (see APPENDIX C). Galvanic coupling at 8.2 kHz, with one lead attached directly to the metal surface of the pipe (exposed by removing the coating) and one lead grounded to a stake in the trench, worked well.

The plot on the top right of FIGURE 14 shows a profile across the oil-o-static trench 570 ft away from the clamp-on point, which was the farthest distance surveyed. (The center of the trench is at $y = 22$ ft on this plot.) As expected, the coils perpendicular to the pipes (channels 2 and 5) receive the strongest signals. The magnetic field is still quite strong at this distance, which indicates that the sensors could track the currents at much even greater distances.

The magnetic field profiles recorded in this survey have a more complicated shape than a profile over a single current-carrying line, which would show a single peak in the horizontal field directly above the current (and a null in the vertical field). In this survey, the magnetic fields are distorted by a metal plate that covers the trench (visible in the photo in FIGURE 14). Even at frequencies in the low kHz range, the metal plate is strong electromagnetic shield, creating a strong shadow and smearing out the magnetic field.

To further study the effect of the steel plate, we surveyed on a dense grid over the pipes twice with the transmitter connected successively to each of the two 10 in. pipe. Contour plots of the horizontal magnetic field (bottom left of FIGURE 14) show that the two different configurations can be distinguished even above the metal plate. Finally, the plot in the bottom right of FIGURE 14 shows a numerical model that includes the effect of shielding by the metal plate in calculation of the magnetic fields at the surface. The calculations match the measured fields in one of the profiles closely, indicating that it would be possible to fix the pipe positions quantitatively by modeling.

3.3 Array Mock Up Test: Newton, Massachusetts

We performed the first test of the fully-assembled EMI system, mounted in the sensor platform, in a parking lot in Newton, MA (FIGURE 15). The towing vehicle was a Chevrolet Tahoe SUV. The survey covered an 80-by-60 foot area, with extension cords laid out on the asphalt to simulate pipes. Current was induced on the extension cords with inductive (toroidal) clamps driven by transmitters operating at 8.2 kHz, 32.8 kHz, and 65.5 kHz. Data was collected along seven straight paths, each roughly 80 feet long, with a frame spacing of 1 ft. Each frame of data consists of 48 channels each containing 5000 time samples. The laser positioning system was not used in this simple “mock-up” test; the survey wheel that triggers the data acquisition provided enough positioning accuracy.

Shown on the right of FIGURE 16 are the combined recorded horizontal magnetic fields at all three transmitted frequencies (8.2 kHz, 32.8 kHz, and 65.5 kHz). We see that the maxima shown in red match the locations of their respective loops qualitatively very well.

3.4 First large-scale survey: November 2003, Southern Connecticut (RWA)

In November 2003, we performed the first large-scale survey (covering about 20 000 sq ft) with the full positioning system. The survey was done for the South Central Connecticut Regional Water Authority (RWA) to track a series of water pipes for their distribution system. Witten Technologies also did a commercial radar survey for RWA of the same area using a 200 MHz CART system, which also allowed the first comparison of the two sets of data. The survey covered a triangular grassy area, about 40 by 250 ft in size and a 300 ft section along the adjacent street.

The GPR data were collected in 41 individual profiles (FIGURE 17a), with one frame of 16 channels collected every 4 inches along the profiles. The raw data were interpolated onto a regular grid (with a grid spacing of 3 in. by 3 in.) before being migrated to a 3D synthetic-aperture image with depth slices at 1-in. intervals down to 72 in. The migration algorithm is a standard integral seismic imaging method adapted for GPR (Oristaglio et al., 2001; Hansen and Johansen, 2000). FIGURE 17b shows a typical depth slice through the 3D image (at a depth of 36 inches). Linear features in underground radar images at this scale generally correspond to buried utility lines or conduits, or to the boundaries of buried trenches containing the lines. The most prominent feature in the image at this depth is a portion of a water line that runs nearly N-S at the southeastern edge of the survey. The full set of image slices, and software for tracking features, allows an interpreter to step through the data volume picking linear features that correspond to possible buried utilities. The picked “pipes” are then exported into a CAD system to compose a final “feature” map – as illustrated in FIGURE 18 – in which the color of lines indicates depth below (local) surface level. Depth can also be referenced to an absolute surface level using 3D positions recorded by the surveying instrument. The feature maps can be converted into subsurface utility maps using other information available (e.g., from engineering plans, from vacuum excavations and test pits) about the size and types of conduits composing the local network. This process has been described in detail in other publications (see Birken et al., 2002).

The EMI survey was done with clamp-on transmitters operating at 4 different frequencies: 8.2, 32.8, 65.5, and 83 kHz. One of the key technical goals of the survey – aside from testing the full system – was to see if currents injected at different frequencies would actually track individual pipes through complicated utility junctions where different utility networks can be in contact, either directly (electrical lines are often grounded onto deep water pipes) or through the soil. FIGURE 19 (left) shows the transmitter clamp-on points. The 8.2-kHz and 83-kHz transmitters were clamped to a valve wrench attached to one of two closely-spaced valves located on a water line underneath the valve cover. The 32.8-kHz transmitter was connected by alligator clip to a water valve inside a manhole bordering the grassy area. The 65.5-kHz transmitter was clamped onto a water pipe within a gate house.

FIGURE 20 shows data collected near the gate house: the plot on the top left shows the horizontal component of the magnetic field at 8.2 kHz measured by sensors on the lower array; the plot on the top right shows the radar image slice at a depth of 17 in. below the surface. The prominent linear feature in radar image is most likely a buried electrical utility line. The peak in the EM field above the pipe is consistent with injected currents on a water line from the 8.2 kHz transmitter flowing along this conduit and leaking into the electrical line. The location is also consistent with the client maps partially shown in FIGURE 19 and the surface locating marks, indicated by orange symbols on the radar image, where were painted on the grass by Call-before-you-dig (APPENDIX B) initiated by RWA to locate these pipes. This locating was probably done with a standard handheld EMI unit.

FIGURE 20 also shows the magnetic field at 32.8 kHz (bottom left) alongside the radar image at a depth of 55 in. The linear feature in these plots is most likely the water pipe indicated on the client map near this location. The agreement between the radar image and the EM data is again impressive. This result, however, is puzzling because we expected from the client maps and the transmitter clamp-on points that this particular water line would be energized with currents at 8.2 kHz, not 32.8 kHz. It is possible that

current at the higher frequency got onto this pipe through a direct electrical contact between these two pipe networks or by leakage through the soil. The positions of the utilities inferred from the radar images and the EM data agree very well, which gives confidence in the absolute positions of the pipes found on these surveys and in the accuracy of the positioning system, since the radar and EM surveys were collected at different times.

FIGURE 21 shows a zoomed in version of the 32 kHz EM data shown at the bottom of FIGURE 20. This data set was matched with a 2D forward model. A comparison between a selected profile across both data sets shows close agreement (FIGURE 21 bottom).

Another comparison between the 8.2 kHz EM and radar data at 24 in. depth, now in the middle section of the grassy area is shown in FIGURE 22. The color scale has been changed so that the areas that were saturated dark red in FIGURE 20 can now be studied. Overlays on the radar images with the client maps (FIGURE 22), however, show differences of up to 8 ft in the horizontal positions of some lines, indicating that at least some features on the maps are incorrect.

Low-frequency interference

Parts of the data were unusable because of high-amplitude magnetic fields at low frequency that exceed the dynamic range of the system and cause the readings to “clip”. FIGURE 23 shows an example. The interfering signals are at about 60 Hz and most likely come from nearby power lines. Overhead lines run along the eastern part of the survey area and along the southern edge of the adjacent street; there is also a large transformer bank near the gate house. In some profiles, the vertical components of the data were more than 95% clipped, meaning there were fewer than 250 uncorrupted samples per trace from which to perform the frequency extraction. These results lead to modifications to the original sensors as described in section 2.1.1, to reduce the sensitivity of the sensors to frequencies below 1 kHz.

3.5 Resurvey of Southern Connecticut site (RWA) with modified sensors

In April 2004, we resurveyed the grassy area with sensors modified to reduce sensitivity to 60 Hz signals. FIGURES 24 and 25 show the results of these tests. Four clamp-on transmitters were placed as shown on the right side of FIGURE 19. Transmitted frequencies are resolved much more cleanly in the data from the modified sensors (compare, for example, FIGURE 20 and FIGURE 24). As noted before, strong linear features in these field maps correspond to narrow highs (or lows) of the field amplitude and provide a good qualitative guide to the locations of buried lines. (The horizontal magnetic peaks directly above a linear current filament; the vertical field is null.) Much more detailed features are visible in the maps made with the new sensors. For example, the horizontal field map at 33 kHz (third plot from left) clearly shows three separate linear magnetic field highs, running approximately N-S, corresponding to currents flowing along three or more buried pipes. At the northeastern end of the survey (upper right of the plot), it appears that the pipe in the middle of the plot (leftmost of the three pipes) bends towards the northwest, but part of the current flows off to the east, perhaps connecting to pipe network running along the eastern portion of the survey. This diversion of part of the current could come from a direct connection between these pipe systems, or could represent “jumping” of the current injected at 33 kHz from one pipe to another by leakage through the soil.

We used data at 9820 Hz from the northeastern part of the survey (near location (80,-50)) to test the inversion software (FIGURE 25). The test area is located near two test pits that were dug by RWA to complete their engineering study. Both the 1D and 3D inversions placed the pipe at a depth of about 71 inches. The test pit in this area uncovered a large (12-in diameter) water pipe a depth of about 66 in. (to the center of the pipe). This accuracy of about 10% is reasonable for a first test in a complicated area.

3.6 Final Field Test: July 2004 Elmsford, NY (Con Edison)

The final field surveys of the Dual Array Project were intended not only to test all the major components of the EMI system, including both the clamp-on and on-board transmitters, but also to simulate as closely as possible a large survey with a true dual-array system combining radar and EMI sensors. To achieve this, two surveys were carried out the nights of August 12 and 13 along a 4-lane wide section of Tarrytown Road (Route 119) in Elmsford, NY. Surveys were carried out “curb to curb” with both the EMI system and the 400 MHz CART radar for a distance of about 1200 ft along Tarrytown Road. The CART surveys covered about 48 000 sq ft; the EMI surveys covered about 39 000 sq ft. A survey covering 77 000 sq ft at the same location was done in 2002 with a 200 MHz CART system. The surveys were conducted for Con Edison’s Westchester Public Improvement division, which was interested in locating and tracking the buried utilities surrounding (and connecting into) a major electrical substation next to the area mapped. The detailed coverage by profiles are shown in FIGURE 26 and 27.

Radar surveys

FIGURES 28-33 show images from the 200 and 400 MHz radar surveys and their interpretation. The radar image slices at 4-in. depth (FIGURE 28a and 29a) show a complicated set of surface features. The bright rectangular areas, mainly in the left half of the image, are reinforced concrete. The rebar structure shows clearly (it appears as the lighter areas in FIGURE 28a), but it also attenuates the radar signal and obscures deeper structures. The right side of the 200 MHz image shows reinforced concrete slabs (see also the 400 MHz image). Additional surface features that can be identified are road cuts and paved over trenches. Roadbed surfaces such as this are common in urban areas and severely complicate the interpretation of radar images. The complications make the site a difficult first full-scale test of the “dual-array” concept, but also highlight the complementary aspects of the radar and EM data.

In the image slices at 27-in. and 30-in. depth (FIGURES 28, 29 and 31-33) several utility lines can be identified at these depths, although in general the quality of the radar images is marginal. This is probably caused by complicated roadbed at the site. The plot at the bottom of FIGURE 29 shows the interpreted utilities overlaid on a map of the surface surveyed with the total station at the time the radar data were collected. The thick red lines outline the areas identified as reinforced concrete. The dashed blue lines are curbs. Individual symbols represent manhole or valve covers, telephone poles, water hydrants or similar surface features, which we also surveyed in with our positioning system. Thin red solid lines outline manhole vaults or shafts. The dashed red lines mark surface trenches. Solid green and blue lines are linear features at depths below 4-in. in the radar image, which could be interpreted as buried utilities.

FIGURE 30 shows a final CAD drawing created from the radar images, with pipes that are now color coded by depth according to the legend at the bottom. Within the CAD software it is now straightforward to create custom views and maps as needed by the client. As part of the Dual Array project, we have written software to import the CAD results into GIS software. Example GIS views are shown in FIGURES 4 and 37.

EMI survey: Clamp-on Transmitter

The EMI surveys used both clamp-on and on-board transmitter. For the clamp-on surveys, transmitters were attached to four different electrical cables in two manholes (FIGURE 27). About a dozen electrical cables run through each of the two manholes. Not all cables are active, and in many cases it is unknown (from maps or records) where the lines extend outside the manhole. One of the goals of the EMI survey – and one of the major commercial applications envisioned by Con Edison – is to track individual lines away from the manhole. For this survey, we energized four cables (two picked at random in each manhole) with toroidal clamps. We expect, however, that the signals will also leak onto nearby cables.

FIGURE 34 shows horizontal surface magnetic field mapped by the sensor array over part of the surveyed area. The contours in the left plot of FIGURE 34 appear to show at least two lines carrying 8.2 kHz current. Lines carrying 32.8 kHz signal can be found more in the southwestern part of the survey. One line parallel to the main street, including a lateral offset, stands out clearly in the bottom part of the data display.

FIGURE 35 shows the horizontal and vertical magnetic fields measured at 65.5 kHz. One interesting feature that shows up frequently in maps of the vertical magnetic field component is a so-called null (zero amplitude) that makes it way clearly through the higher amplitudes around it. This is a strong indication of a pipe right underneath, because on top of a pipe the vertical magnetic field component is zero. Looking at the map on the right of FIGURE 35 one can follow the continuation of a pipe (shown in bottom half of FIGURE 34) towards the Northwest through the high amplitudes in the center of map. We selected data from the area outlined in red for inversion.

FIGURE 36 shows the results of the inversion, fixing the horizontal and vertical position of the pipe in this area. We believe that the horizontal location and depth of what is believed to be a gas pipe is very well determined.

The right map in FIGURE 37 is a GIS composition of the copperscale 200 MHz radar image in the background, overlaid with the horizontal magnetic field component of the 65 kHz EM data (compare to FIGURE 35). On top of the data images we display the qualitative pipe picks from the EM data in thicker gray lines, the pipes identified based on the radar data in thin lines color coded by depth, miscellaneous surface features (symbols) and the curbs. In these kind of displays or software one can now directly compare the results of the radar and EM method.

The CAD layouts in FIGURES 31-33 illustrate the complementary aspect of the EM and radar data. These plots compare of EM data at 65 kHz and 32 kHz EM data with the 200 MHz data at 30 in. depth. Consider, for example, FIGURE 32. The radar image clearly shows a pipe parallel to the street (bottom right of the image). The corresponding area in the EM data map shows a linear ridge of high magnetic field (indicated by a light blue color). While there are gaps in the radar image, the EM data map leaves no doubt where the pipe is located. In the center of the maps, a trench (outlined in red) is bending up by about 45 degrees. In the radar image one detects a weak presence of a pipe inside the trench. The EM data clearly show the line, because it actually carries a strong EM signal. Now in the EM data one can also see a green-blue pipe that almost forms a closed loop with the one just described. This electrical cable picked up the transmitted signal and can now be located as well, while it's presence isn't clear in the radar data at this or any other depth. On the other hand the radar data shows many other pipes that are not energized with an EM signal (FIGURE 33) or that are not a conductor such as PVC pipes.

EMI survey: On-Board Transmitter

The survey at Elmsford was the first major field test using on-board transmitter (section 2.2.2). In the course of this survey, we identified three problems with the prototype system: 1) variations in transmitter orientation, 2) weak reference signal strength, and 3) phase instability.

During surveying, the transmitter was suspended from the back of the AIR array using a carbon-fiber rod. The first night it was laterally secured using nylon tie-rope. In this configuration the transmitter could move up to a foot in the vertical direction with the movement of the system due the flex of the carbon-fiber rod (FIGURE 27). The second night a support was added beneath the transmitter which greatly improved its stability. However, a more robust and permanent system needs to developed. This problem can easily be fixed with the proper mounting design.

Further study of the on-board data collected at Elmsford also showed that the signal from the reference coil pod was too weak to be recorded properly by the DAQ system. This problem was fixed by adjusting

the gain on the DAQ and by using an in-line amplifier. FIGURE 38 illustrates the problem and its solution. Plots on the left of the figure show a section of data as recorded from the reference coil during the Elmsford survey; plots on the right show reference channels collected in the lab after adjusting the gain in the DAQ and using the in-line amplifier. We can see that the reference signal is now fully resolved.

The third and most serious problem was the discovery of phase instability in the system. This is caused by the Yokogawa DAQ system itself. To determine this, a series of tests were performed back in the lab. First, data was collected with the AIR system in a stationary position. The phase difference between the reference channel and a given channel for different time triggers was calculated. The top of FIGURE 39 shows the results for the phase difference between channel 48 (the reference channel) and channel 4 for the stationary system. Theoretically, this difference should be constant. However, we see here the phase changes by as much as 8 degrees. As a comparison we conducted a similar experiment using a Yokogawa Oscilloscope as the data acquisition device. The bottom of FIGURE 39 shows the results from this experiment. Here we see that there is a maximum phase difference of about 0.04 degrees, which is what one expects to observe. This is evidence that the problem is with the Yokogawa DAQ and its internal "simultaneous" triggering. This problem can be addressed by replacing the Yokogawa DAQ with another system or by having a custom made DAQ system.

In addition, a theoretical model of the on-board system was developed in order to predict the range of experimental results possible. FIGURE 40 shows the geometry of the system used for this model. The model system closely matches the actual configuration of the on-board system. It also shows the magnitude of the amplitude and phase response for a 20 cm diameter pipe buried at a depth of 1 meter. A 3 degree change in the phase is predicted for a buried pipe. This illustrates the importance of having stable phase measurements. If there is inherently an 8 degree phase variation in a stationary position, then there is little chance a buried pipe can be detected using the phase information. However, there is no fundamental problem why a stable system can not be produced (as shown in this section). Therefore, we feel with the correct electronic hardware and stable geometry between the on-board transmitter and receiver array a reliable on-board system can be assembled.

Despite these problems, we were still able to get useful qualitative information out of the onboard data. Phase extraction was not possible because the signal from the reference channel was poor, as discussed above. Therefore, a different processing approach was taken. The median amplitude was subtracted for each profile. This in effect removes the primary field from the data set, leaving only the induced fields, which are produced by conductive features. FIGURE 41 shows the three recorded magnetic field components at the on-board transmitter frequency of 22.8 kHz. The contours correspond to the rebar throughout the street. These same features were found in the 200 MHz and 400 MHz radar data at those locations. Secondly, proof that these contours are not an artifact, is the areas of high amplitude (red color) is confined to the center of the road, where the rebar is located and is not seen in the areas near the curb, where there should not be any rebar (compare to FIGURE 30).

3.7 Field Test Assessment

The field tests accomplished the main goal of the development project which was to demonstrate feasibility of the concept of mapping EM fields at multiple frequencies over large areas with a broadband EMI array. The side-by-side tests with the CART radar system also demonstrated the feasibility of the "dual-array" concept. The field tests for RWA and Con Edison are (we believe) the first large-scale surveys for infrastructure mapping combining multi-frequency EM data with high-resolution radar images.

The tests also highlighted areas where further development work is needed. The main development area for the EMI array is in automation of the software processing chain, especially the steps leading to creation of maps for comparison with (or integration into) maps created by radar images. The inversion software is working, but setting up the inversion model is time-consuming as it requires entry by hand of

the starting model, which is only practical for small areas. Software already used in the CART data processing chain to track the locations of pipes can easily be adapted to determine a starting model for the full inversion. FIGURE 37 shows two examples, with approximate pipe locations picked by tracking features in the EM data superimposed on the data map and an aerial photograph.

More study is needed to understand the issues related to leakage of current between different buried pipe networks. The inversion model and software was designed to handle these complications, but will require further testing to demonstrate its practical limits. For example, the nominal accuracy of about 10% in depth location, achieved in the field tests, can probably be improved dramatically (to 2 to 3%) given the precision of the sensors and the positioning system.

The hardware for the EMI array EXP performed up to its specifications, with the exception of the phase control for the on-board transmitter (see previous section). Further tests with the Yokogawa DAQ system are planned to determine whether the phase inaccuracy is a fundamental limitation of the Yokogawa system or can be removed by re-wiring the control electronics or changing the triggering. In any event, a new integrated DAQ board should be designed for the ENP (section 4) to handle all 48 channels in a more compact, and cheaper, system.

4 Commercialization Issues

4.1 Dual-array engineering prototype

This section discusses some improvements that could be made in building an engineering prototype (ENP) of the dual-array system, which can serve as a template for a commercial product. No new technology needs to be developed for the ENP; as demonstrated by the final field tests, the technical specifications of the sensors and transmitters, and the capabilities of the software, are sufficient for commercial work. The system itself in its current packaging is, however, not rugged or reliable enough for routine commercial work. The most significant practical improvements would come from two areas: (1) better packaging of the sensor arrays (radar and EMI) into an integrated system that would increase efficiency in the field and (2) further refinement of the software to automate the tasks of producing final electronics maps. In addition, ENP development should improve the positioning system by integrating tilt sensors and a GPS. TABLE 4 summarizes the estimated cost for development of an ENP at about \$1.2 million. The minimum time for development is estimated about 12 months, assuming all of the individual developments listed could be done in parallel; a more reasonable estimate would be 18 months.

Table 4. Cost Estimate for ENP Development

	man-mos	Cost (k\$)
EMI Sensor Array		
Design and develop new EMI DAQ board	9	250
Radar Improvements		
Improve radar antennas and electronics*	12	250
Integrated Vehicle for Dual-Array system		
Design and build vehicle with new trailer for EMI array	6	120
Develop new positioning system with GPS, geodimeter, and tilt sensors	6	120
Develop data acquisition system for radar and EMI arrays	6	80
Commercial Software Package		
Automated commercial inversion software for EMI array	12	120
Integrated radar and GPR processing chain (in MATLAB)	12	120
Automatic Feature Extraction and Map Creation in GIS	12	120
TOTALS	75	1,180

*Done with existing partner, Mala Geoscience

TABLE 5 in the section on Cost-Benefit analysis gives an estimated cost of about \$160k for a full Dual-Array ENP if produced in limited quantities (5 units). The cost is split almost equally between the radar and EMI arrays. Prices are based on actual current costs for the different hardware components, obtained from the manufacturers. These costs can, of course, be reduced substantially (probably by 50%) if the systems are manufactured in large quantities (50 units a year). The cost of other equipment (vehicle, positioning system, and computers) and software to fully operate the system is about \$100k for a total capital asset cost of about \$260k.

4.1.1 Sensors: Radar and EMI arrays

No significant new developments are needed for the EMI sensors. Some improvements would be made in packaging of the sensors (reduction of size and weight) and in the control electronics, including adjustable pre-amplifiers and filters. In addition the custom built on-board transmitter won't need significant new developments, just a few minor improvements to the control software and reference signal.

Substantial improvements can be made in the packaging of the radar antennas and electronics. The entire radar could be substantially reduced in size and weight. In addition, better broadband antennas can now be fabricated that operate in dual-frequency ranges. These improvements could be made directly to the CART system, which is based on the first commercial array radar built by Malå Geoscience. In addition, new GPR arrays are now being offered commercially by different manufacturers. The software for the CART and dual-array system can easily be adapted to any of these systems.

4.1.2 Data acquisition

An integrated DC-powered data acquisition board should be designed and built for the EMI array. This will involve a repackaging of the electronics for the Yokogawa system, whose specifications are sufficient for commercial work with clamp-on transmitters. (Realizing the full specifications will also require improvements in the control software.) However, the Yokogawa system would have to be reevaluated with respect to the on-board data collection as discussed in section 3.6.

The capabilities of commercial DAQ systems are, however, still not sufficient for real-time digitization of GPR waveforms, which require sampling rates of 10 GHz (or more). Pulsed GPRs like the CART record only one sample of the waveform each time the source is fired; the source is fired repeatedly to build up the full waveform. A small project should be done to look at the latest generation of fast ADCs (which can digitize at about 50 MHz) and evaluate whether it would be possible at reasonable cost to build a GPR that can digitize the entire waveform in real time by running a suite of fast ADCs time shifted.

4.1.3 Positioning system

Laser positioning with a total station is still the preferred solution for (x,y,z) positioning to accuracy standards required in construction and civil engineering. The accuracy of the total station used for the EXP field tests is sufficient for commercial work, but its rate of data acquisition currently limits the speed of the vehicle to about 10 mi/hr. This would be acceptable for most commercial mapping services, but would ultimately limit the capabilities of the system for large-scale infrastructure mapping. New “robotic” total stations can provide improvements in speed, accuracy, and logistics of positioning, but at increased cost. The most important technical improvement in positioning will be the addition of inclinometers to sense and record the tilt of the sensor arrays, which is needed for true 3D work on rough terrain. Commercial inclinometers costing about \$2k per sensor are capable of producing the accuracy needed for nearly all applications.

A GPS system for absolute positioning should be integrated into the data acquisition for absolute positioning. GPS continues to make steady improvements in accuracy, speed, and reliability and should eventually provide an alternative to laser positioning. In fact, the specifications for the most advanced GPS systems using Real-Time-Kinematic (RTK) technology is already good enough for use with a commercial dual-array system, but the cost of these systems is very high (in the range of \$100k or more).

In addition a video system recording the surveyed area should be integrated as a visual geometry data stream.

4.1.4 Vehicle

A new vehicle is needed to deploy the dual-array system. The most natural configuration would be a vehicle with the radar deck mounted on the front and the EMI sensor bookcase mounted on the back (or deployed on a towed trailer). Two versions should be considered a road version, which could utilize a small van, and an off-road version similar to the tractor used in the existing pushed CART system.

4.1.5 Data processing and data management system

A major part of the development effort for the ENP will involve software engineering of the processing chain. Although all of the major components of the software have been coded and tested, significant improvements can be made in the user interface and in automating the data analysis to create final maps in CAD or GIS. This step is currently the most time-consuming part of the processing.

4.2 Cost-benefit analysis

Background and Overview

This section outlines a cost-benefit analysis of underground mapping with the Dual Array system. The key ingredients of the analysis are described and several scenarios are studied using typical figures for the size, cost and possible benefits of large-scale underground mapping. One of the difficulties with this exercise is that there is no established market for large-scale (non-invasive) 3D underground mapping services in the utility and construction industries. In fact, until recently it was impossible to carry out such surveys at reasonable time and cost. Nevertheless, the value and benefits of mapping before construction have been established, mainly through systematic studies in connection with the nationwide One-Call system and the emerging professional engineering discipline called Subsurface Utility Engineering (SUE). Two recent articles by Jeong et al. (2003, 2004) are excellent up-to-date descriptions of the complementary aspects of the One-Call system and SUE. One-Call is mainly directed at preventing accidents during actual digging by requiring that utility companies mark the locations of buried utilities in advance of construction. SUE is directed mainly at improving the design and engineering process of any construction project that could impact buried utilities. Many of these projects involve highway construction, which is why the U.S. DOT and Federal Highway Administration (FHWA) have played major roles in the promotion of SUE. TABLE 5, taken from Jeong et al. (2003), compares the activities in One-Call and SUE.

Table 5. Comparison of One-Call and SUE (Jeong et al., 2003)

Item Description	One-Call	SUE
Use	Excavation activity based	Typically project based
Applied stage	During construction	During design and engineering
Obligation	By state law	No obligation
Range of service	2D horizontal location	2D/3D (including depth)
Deliverables	Marking on the surface	Transferring data obtained into project plans, typically in electronic form
Accuracy/Quality	Relatively low	Relatively high (esp. for levels B, A)
Work solicitation practice	Bidding - lowest bidder	Typically negotiation
Major contract method	Unit price	Cost-plus-fee and unit price
Major benefits	Avoidance of accidents (pipeline hits)	Construction cost savings, avoidance of pipeline hits, higher accuracy, electronic data archiving
Major disadvantages	Relatively low accuracy, not useful for advance planning or as cost saving tool	Higher cost

The dual-array system is a prototype of the next generation of geophysical technology for more efficient, comprehensive, and accurate shallow underground mapping. One of the key goals in its development was to produce a system that could create infrastructure maps over large areas in a form that allows their archiving electronically in geographic information systems (GIS). Although this technology has applications in One-Call Systems, the economics of its introduction to the marketplace fit better into the activities called SUE quality levels B and A (Stevens and Anspach, 1993; Lew, 1996; ASCE, 2002):

Quality level D consists of information derived from existing records or verbal recollections.

Quality level C consists of information obtained by surveying and plotting visible (above-ground) utility features and by using professional judgment in correlating this information to Quality Level D information.

Quality Level B involves the application of appropriate surface geophysical methods to determine the existence and approximate horizontal position of subsurface utilities. The subsurface information obtained in level B is surveyed to applicable tolerances defined by the project and imported onto plan documents.

Quality Level A provides precise horizontal and vertical location of utilities obtained by actual exposure (or verification of previously exposed and surveyed utilities) and subsequent measurement of subsurface utilities at specific points. The 3D data of location, as well as other utility attributes (e.g., type of utility and size and composition of conduit), are shown on plan documents. Accuracy is typically 15 mm vertical and set at applicable horizontal survey and mapping accuracy levels as defined or expected by the project owner.

The technology in the dual-array system can, in fact, help to merge SUE levels A and B into a more seamless activity, by allowing accurate geophysical mapping over large areas efficiently and by providing (nearly) continuous depth information with more accuracy than previous technologies. An important part of this improvement comes from having independent measurements of depth and horizontal location in a single geophysical system. In addition, the complementary nature of radar and induction will allow operation in more soil types than either technology alone.

Achieving SUE Quality level A at present requires (by definition) exposure of underground utilities, which is done by either careful hand digging or vacuum excavation. This is at present the only way to achieve the extreme vertical accuracy required for level A data, or to obtain auxiliary information about utilities (type, size, and composition). The images and feature maps that can be obtained with the dual-array system can, however, be used to target the best locations for vacuum, reducing the number of holes needed to achieve an accurate subsurface picture. Also, the information obtained from excavation can be used to calibrate the depths of radar and EMI and then interpolated over the entire survey area. Techniques for doing this are already well-developed in oil and gas exploration to interpolate rock properties obtained from borehole logs over the entire reservoir using 3D seismic images.

4.2.1 Cost Analysis of 3D Mapping with Dual Array System

The natural unit for pricing geophysical mapping services with the dual-array system is per square foot of area mapped. The goal of mapping is to cover all accessible areas, and for large areas, costs of acquiring data and producing final maps scale almost linearly with area covered. In this section, we estimate the cost per square foot of a 3D mapping service with the Dual Array system using the cost estimate for the ENP and assumptions about personnel costs consistent with our experience with 3D mapping using the CART system.

TABLE 6 summarizes these costs. We assume that a mapping service with the Dual Array system will initially require a staff of four for each system: a field crew of two to acquire data and an office staff of two to process the data and produce final maps. These personnel costs are by far the largest item in the monthly cost structure. The hardware cost is based on current cost of the radar array in the CART System (about \$80k) and an estimated cost (also about \$80k) for a commercial EMI array. The price for the software reflects a large effort over several years to develop the data processing, imaging and visualization software. Both hardware and software costs can come down significantly if amortized over a large number of systems. The monthly cost assumes a depreciation life of 36 months, which is reasonable for all major system components.

These figures give a breakeven point for one CART system and crew at monthly revenues of about \$50k. A reasonable production rate during introduction of the technology is about 450 000 sq ft per month, or about 15 service days per month at 30 000 sq ft per day. The estimated breakeven cost of 3D mapping service with the dual-array system is thus about \$0.11 per square foot covered. These are consistent with the costs for CART mapping services. Witten Technologies and licensees of the CART system typically charge between \$0.20 to \$0.50 per square foot for CART surveys, depending on the urgency of the job, the complexity of the area covered, and the level of detail required in the final maps.

Table 6. Dual Array Economics

Monthly Cost (\$)	49,521	Capital Assets (k\$)	257.3
Salaries (2 field engineers, 2 data processors)	18,000	Radar array	76.0
Benefits (25%)	4,500	Controller	20.0
Overhead and G&A (65%)	14,625	Antennas	51.0
Depreciation (over 36 months)	7,146	Deck	5.0
Data Processing Expenses	1,750	EMI array	80.5
Field Expenses Local	2,000	DAQ system	25.0
Contingency	1,500	Magnetometers	48.0
		Sensor bookcase	7.5
		Other equipment	67.5
Daily Production rate (sq ft)	30,000	Vehicle	30.0
Service days per month	15	Positioning system	30.0
Sq ft surveyed per month	450,000	Field computer	2.5
Cost per sq ft	0.11	Data processing computer	5.0
		Software	33.3
		Dual-Array software	25.0
		MATLAB	3.0
		CAD	3.8
		GIS	1.5

The nominal cost of 3D mapping with the dual-array system, calculated TABLE 6, can be compared with typical costs in subsurface utility engineering (SUE). TABLE 7, from Jeong et al. (2004), summarizes these costs based on responses to a survey in 2003 of SUE companies in the U.S. The 21 respondents to this survey (out of 45 companies sent questionnaires) represented about \$80 million in total annual revenues, which was estimated to be about 80% of the total market for SUE services in 2003.

SUE services for “utility designating” – locating the horizontal position of utility lines using geophysical methods – are generally charged per linear ft (or linear m) of utility mapped and average about \$1.17/ft (\$3.84/m). If we assume that these charged costs include a markup of 20%, we arrive at a typical SUE cost of \$1/ft. To compare these costs with 3D mapping, we need to make some assumptions about the total length of utility lines per surface area covered. Consider, for example, an area 100 ft wide by 100 ft long. A 3D survey to map this 10,000 sq ft area with a Dual-Array would cost about \$1,200 (at breakeven). If 1100 linear ft of utility line is located under the 10,000 sq ft of area, 3D mapping costs are comparable to typical SUE costs (\$1,100/1000 ft = \$1.10/ft). A density of .11 linear ft of utility line per sq ft of surface area is not unusual in utility corridors or areas surrounding industrial plants. For example, the Elmsford survey for Con Edison covered a total of 77 000 sq ft and mapped about 5400 ft of utilities, corresponding to an average density of 0.14 linear ft per sq ft of surface area.

Table 7. SUE Productivity and Cost* (Jeong et al., 2004)

Subsurface utility engineering activity		Mean	Standard Deviation	Minimum	Maximum	Crew
Designating (geophysical mapping)	Productivity (m/day)	994	794.6	250	3 333	2
	Unit cost (\$/m)	3.84	2.389	0.75	11.25	
Locating (non-destructive excavation)	Productivity	6	2.0	4	12	3-4
	Unit cost (\$/hole)	560	442.9	300	2 500	

*Based on responses from 21 SUE companies (out of 45 surveys distributed), representing about \$80 million in annual revenues.

4.3 Commercialization Strategy

The next key step for commercialization of the dual-array system is setting up a project to develop an ENP. We believe that this project would best be done in a way similar to the EXP development; that is, through a development contract sponsored by government and industry funding. Now that feasibility of the concept has been demonstrated, it should be possible to expand the number of cost-sharing partners, thereby reducing the financial contribution of each partner to a modest level. For example, six partners contributing about \$100k each in two fiscal years would finance the \$1.2 million development cost estimated for the ENP development.

So far, Witten Technologies has pursued a service business model in introducing advanced technology for large-scale underground mapping (such as the CART Imaging System) to the marketplace. As described in the previous section, the mapping rates (in \$ per sq ft) are competitive with other technologies and services currently used in construction planning. We believe that this model can still be used for the dual-array system, both directly by Witten Technologies and by its licensees. In fact, the ability of the complementary technologies in the dual-array system to work in nearly all soil types down to significant depths should make it more attractive for licensing by SUE and other engineering firms interested in applying advanced new geophysical technology to construction engineering. Further experience with the ENP in a broader range of applications will be needed before the dual-array system could be considered as a complete integrated technology for sale and use by “end-users” such as utility or construction companies.

A key to introducing the technology to the marketplace will be a demonstration of its capabilities in large-scale projects. One way to accomplish this would be a demonstration project to map a large section of an underground network in a major metropolitan area. For example, a fleet of five dual-array ENPs could map most of downtown Washington, DC, in a project lasting about 24 months. Again, a natural way to fund such a project would be through a consortium of government and industry partners.

5 Financial Summary

TABLE 8 below summarizes the original plan, which called for a project extending over 8 quarters with the major milestones as listed. At the end of 2003, WTI requested from USDOT – and was granted – an extension of the project by one quarter including an increase of the overall budget from \$944,128 to \$1,008,731.20.

TABLE 8: Original Proposed Technical and Deliverable Milestone Schedule						
		<u>Expected</u>		<u>Projected</u>	<u>Projected</u>	
	<u>Quar-</u>	<u>Completion</u>		<u>Federal</u>	<u>Partner</u>	
<u>Activity/Deliverable</u>	<u>No.</u>	<u>Date</u>	<u>Payable Milestone</u>	<u>Payment</u>	<u>Sharing</u>	<u>Total</u>
<u>ACTIVITY/DELIVERABLE</u>			<u>TITLE</u>			
Development of 6-channel prototype: Acquire electronics equipment and hardware	I	Oct-02	Acquire and install electronics equipment	25,516	29,358	54,874
Development of 6-channel prototype: Design and assembly	I	Nov-02	6-channel prototype assembled	1,886	2,170	4,056
Development of 6-channel DAQ software	I	Nov-02	Functional DAQ software	6,529	7,511	14,040
Testing of 3-component sensor	I	Nov-02	Satisfactory sensor behavior	1,378	1,586	2,964
Initial processing and interpretation software with clamp-on sources	I	Nov-02	Software verified with synthetic data	7,254	8,346	15,600
Interface between DAQ and processing software	I	Nov-02	DAQ data format compatible with processing software	551	634	1,186
Field testing	I	Dec-02	Completion of experiments A-D for phase 1.	3,409	3,923	7,332
Quarterly Status Report	I	Dec-02	Submit quarterly report	1,539	1,770	3,309
First Payable Milestone	I	Dec-02	SUBTOTAL	48,063	55,298	103,360
Evaluate and acquire DAQ hardware for full system	II	Jan-03	Acquire and install DAQ hardware for full system	27,829	32,019	59,848
Assemble DAQ hardware for full array	II	Feb-03	DAQ hardware assembled	522	601	1,123
Fabrication of 3-component sensors	II	Mar-03	Sensors delivered	82,681	95,127	177,808
Development of mounting frame and vehicle	II	Ongoing	Initial design completed	12,318	14,172	26,490
Development and Assembly of full array	II	Ongoing	Full array connected to DAQ	2,611	3,005	5,616
Development of DAQ software for full array	II	Ongoing	Initial functionality implemented	7,834	9,014	16,848
Full data processing and interpretation software for clamp-on sources	III	Ongoing	Initial functionality implemented	10,192	11,726	21,918
Quarterly Status Report	II	Mar-03	Submit quarterly report	569	654	1,223
Second Payable Milestone	II	Mar-03	SUBTOTAL	144,556	166,318	310,874
Development of mounting frame and vehicle	III	May-03	Mounting frame and vehicle assembled	12,579	14,472	27,051
Development and Assembly of full array	III	May-03	Full array system assembled	3,264	3,756	7,020

Development of DAQ software for full array	III	May-03	Functional DAQ software for full array	5,223	6,009	11,232
Software to merge positioning information and array data	III	Apr-03	Software verified with synthetic data	6,845	7,875	14,720
Full data processing and interpretation software for clamp-on sources	III	Jun-03	Software verified with synthetic data	8,777	10,099	18,876
Development of software interface to CAD	III	Ongoing	Software verified with synthetic data	3,552	4,086	7,638
Development of software interface to GIS	III	Ongoing	Software verified with synthetic data	13,601	15,648	29,249
Field testing	III	Jun-03	Completion of experiments A-D for phase 2. See Field Test task table (Attachment 4).	4,649	5,348	9,997
Quarterly Status Report	III	Jun-03	Submit quarterly report	1,120	1,289	2,409
Third Payable Milestone	III	Jun-03	SUBTOTAL	59,609	68,583	128,192
Development of software interface to CAD	IV	Aug-03	Software verified with real data from field tests	1,451	1,669	3,120
Development of software interface to GIS	IV	Aug-03	Software verified with real data from field tests	7,091	8,158	15,249
Integration of radar and EM arrays with one vehicle	IV	Aug-03	Systems mounted on single vehicle	8,709	10,019	18,728
Development of common power supplies and triggering systems	IV	Aug-03	Common power supply and triggering system installed	4,935	5,677	10,612
Software for combined visualization and interpretation of EM and radar data	IV	Ongoing	Software verified with real data from field tests	7,363	8,471	15,834
Field testing	IV	Sep-03	Completion of experiments A-B for phase 3. See Field Test task table (Attachment 4).	7,424	8,541	15,965
Quarterly Status Report	IV	Sep-03	Submit quarterly report	1,120	1,289	2,409
Fourth Payable Milestone	IV	Sep-03	SUBTOTAL	38,091	43,825	81,917
Modeling and inversion to design transmitter geometry specifications	V	Nov-03	Geometry design completed	5,803	6,677	12,480
Development of on-board transmitter: Acquire hardware for transmitter coils and electronics	V	Nov-03	Acquire hardware for transmitter and electronics	8,567	9,857	18,424
Software for combined visualization and interpretation of EM and radar data	V	Nov-03	Software verified with real data from field tests	7,363	8,471	15,834
Software interface from combined interpretation to CAD	V	Nov-03	Software verified with real data from field tests	1,451	1,669	3,120
Software interface from combined interpretation to GIS	V	Nov-03	Software verified with real data from field tests	5,731	6,593	12,324
Development of on-board transmitter: Design and Assembly of on-board transmitter	V	Dec-03	Functional on-board transmitter assembled	5,223	6,009	11,232
Addition of channels to DAQ system and modifications to DAQ software to record phase of transmitter currents	V	Dec-03	Functional DAQ software for on-board transmitter	5,223	6,009	11,232
Full data processing and interpretation software for on-board transmitter	V	Ongoing	Software verified with synthetic data	5,803	6,677	12,480
Quarterly Status Report	V	Dec-03	Submit quarterly report	1,120	1,289	2,409

Fifth Payable Milestone	V	Dec-03		46,284	53,251	99,535
Integrate on-board transmitter with vehicle	VI	Jan-04	On-board transmitter integrated with system	6,238	7,178	13,416
Full data processing and interpretation software for on-board transmitter	VI	Mar-04	Software verified with real data from field tests	11,606	13,354	24,960
Field testing	VI	Mar-04	Completion of experiments A-E for phase 4. See Field Test task table (Attachment 4).	10,798	12,423	23,221
Quarterly Status Report	VI	Mar-04	Submit quarterly report	1,539	1,770	3,309
Sixth Payable Milestone	VI	Mar-04	SUBTOTAL	30,181	34,725	64,906
Identification of Commercial Field Test Sites	VII	Apr-04	Identified sites	2,350	2,704	5,054
Cost-Benefit Analysis	VII	Ongoing	Accumulate data and sources for analysis	10,446	12,018	22,464
Final commercial field tests	VII	Jun-04	Field test completed	8,658	9,961	18,619
Creation of utility maps of field test sites in CAD and GIS formats	VII	Ongoing	Drafts of utility maps	4,969	5,717	10,686
Outline of Final Report	VII	Jun-04	Initial table of contents	1,625	1,870	3,494
Quarterly Status Report	VII	Jun-04	Submit quarterly report	1,120	1,289	2,409
Seventh Payable Milestone	VII	Jun-04	SUBTOTAL	29,168	33,559	62,727
Cost-Benefit Analysis	VIII	Jul-04	Cost-Benefit Analysis completed	3,768	4,335	8,103
Creation of utility maps of field test sites in CAD and GIS formats	VIII	Jul-04	Submit utility maps	4,244	4,882	9,126
Final Report: First Draft sent out for review	VIII	Jul-04	Submit final report for review	16,368	18,832	35,200
Guidelines for use of remote sensing in pipe mapping and inspection	VIII	Sep-04	Submit guidelines	4,762	5,478	10,240
Final Report and Documentation Complete	VIII	Sep-04	Submit final report	4,370	5,028	9,398
Outreach presentation and workshop	VIII	Sep-04	Hold the workshop	8,018	9,224	17,242
Quarterly Status Report	VIII	Sep-04	Submit quarterly report	1,539	1,770	3,309
Eighth Payable Milestone	VIII	Sep-04	SUBTOTAL	43,067	49,550	92,617
			GRAND TOTALS	\$ 439,019	\$505,108	\$ 944,128

The project will finish in December 2004, having met all its major milestones. Throughout the project the actual spending deviated slightly from the proposed spending driven by the progress of the project. However, by the end of the final ninth project quarter the deviations in the personnel cost versus the equipment and supplies cost offset each other and the project concluded within the extended proposed budget of \$1,008,731.20.

As the project concludes it is worthwhile to look at the amounts spend throughout the 9 quarters of the project. TABLE 9 shows the total actual spending by quarter. The total per quarter is broken out in two ways. First split into the federal and cost-share partner amounts and second into four columns of

personnel cost, benefits and overhead, equipment and supplies, and travel. The differences in the last four columns (last row of TABLE 9) offset to \$0.00. While the actual spending in each quarter wasn't identical to the proposed spending it all offset at the end after nine quarters, as the actual match the proposed federal and cost-sharing partner amounts.

TABLE 9

<u>Project Quarters</u>	<u>TOTAL</u>	<u>Federal Payment</u>	<u>Partner Cost-Sharing</u>	<u>Personnel Cost</u>	<u>Benefits & Overhead</u>	<u>Equipment & Supplies</u>	<u>Travel</u>
Q1	\$ 57,307.60	\$ 26,648.03	\$ 30,659.57	\$ 34,822.22	\$ 14,068.18	\$ 8,417.20	\$ -
Q2	\$ 219,158.61	\$ 101,908.75	\$ 117,249.86	\$ 41,833.33	\$ 16,900.67	\$ 160,168.61	\$ 256.00
Q3	\$ 113,161.19	\$ 52,619.95	\$ 60,541.24	\$ 60,855.56	\$ 24,585.64	\$ 27,263.16	\$ 456.83
Q4	\$ 82,447.55	\$ 38,338.11	\$ 44,109.44	\$ 49,894.44	\$ 20,157.36	\$ 12,150.75	\$ 245.00
Q5	\$ 70,992.91	\$ 33,011.70	\$ 37,981.21	\$ 47,016.67	\$ 18,994.73	\$ 4,286.31	\$ 695.20
Q6	\$ 123,772.65	\$ 57,554.28	\$ 66,218.37	\$ 68,580.67	\$ 27,706.59	\$ 23,512.50	\$ 3,972.89
Q7	\$ 126,309.69	\$ 58,734.01	\$ 67,575.69	\$ 60,289.69	\$ 24,357.03	\$ 38,947.90	\$ 2,715.07
Q8	\$ 97,204.29	\$ 45,200.00	\$ 52,004.30	\$ 64,843.63	\$ 26,196.83	\$ 4,086.47	\$ 2,077.37
Q9	\$ 118,376.71	\$ 55,045.17	\$ 63,331.54	\$ 69,588.32	\$ 28,113.68	\$ 19,605.89	\$ 1,068.82
Total spent:	\$ 1,008,731.20	\$ 469,060.01	\$ 539,671.19	\$ 497,724.52	\$ 201,080.71	\$ 298,438.79	\$ 11,487.18
Total proposed:	\$ 1,008,731.20	\$ 469,060.01	\$ 539,671.19	\$ 456,048.53	\$ 184,243.61	\$ 355,986.03	\$ 12,453.03
Difference:	\$ (0.00)	\$ (0.00)	\$ (0.00)	\$ 41,675.99	\$ 16,837.10	\$ (57,547.24)	\$ (965.85)

6 Acknowledgement

A large number of people have contributed to the ideas and technology used in the Dual-Array Project. Some of the original concepts for inverting electromagnetic induction measurements to complement ground-penetrating radar images were developed in the Ground-Penetrating Imaging Radar Project at Schlumberger, which was partly sponsored by EPRI. The original members of the GPiR team were Paul Albats, Maclyn Burns, Anthony DeRubeis, Jakob Haldorsen, Thorkild Hansen, Douglas Miller, and Michael Oristaglio. This group joined Witten Technologies in May 2000, and along with Ross Deming, Robert Casadonte, and Ralf Birken was the technical team that commercialized the imaging radar used in the CART system. This group also developed the first version of the positioning system and mobile sensor platform that was adapted for the EMI array during the Dual-Array project. Others who contributed to the field testing of the CART and EMI system include Witten field engineers Andrew Thoms, Andrew Farhat, Tuna Uluaydin, and Rodney Nedd.

Richard Stearns and John Conniff at Witten's data processing center in Austin processed and interpreted radar data covering hundreds of thousands of square feet and created engineering CAD drawings of the results.

The following Dual-Array Project team members were instrumental in creating and testing the EMI array system, integrating it with the radar array and in completing the project successfully in time (listed in alphabetical order):

- Ralf Birken Technical and administrative project management; Radar and EM software development, data acquisition, processing and interpretation; EM system hardware development and maintenance; report writing
- Rob Casadonte Radar data acquisition, processing and interpretation; CAD work
- Ross Deming Radar and EM software development, data acquisition, processing and interpretation
- Thorkild Hansen Radar and EM software development; EM data acquisition, processing and interpretation; report writing
- Theresa Kennedy Development of CAD to GIS interface; GIS work
- Scott MacIntosh EM system hardware development and maintenance; EM software development, data acquisition, processing and interpretation
- Michael Oristaglio Technical and administrative project management; Radar and EM data acquisition and interpretation; report writing
- Rich Stearns Radar data processing and interpretation; CAD work
- Tuna Uluaydin Radar data acquisition and processing; EM system hardware development and maintenance; CAD work
- Qifu (Steve) Zhu Radar and EM software development, processing and interpretation

Finally, Marian Gandire helped with many of the organizational and financial details of the project as Witten Technologies Human Resources Administrator and office manager.

7 References

- Anspach, J. H., 1995, Subsurface utility engineering: Upgrading the quality of utility information: Proc. Conf. on Adv. in Underground Pipeline Eng. II, 2nd Int. Conf. ASCE, New York, 813-824.
- ASCE, 2002, Standard guidelines for the collection and depiction of existing subsurface utility data: ASCE C-1 38-02, New York.
- Bernstein, R., Oristaglio, M., Miller, D., and Haldorsen, J., 2000, Imaging radar maps underground objects in 3D: IEEE Computer Applications in Power, July, 20-24.
- Birken, R., Miller, D., Burns, M., Albats, P., Casadonte, R., Deming, R., DeRubeis, T., Hansen, T. and Oristaglio, M., 2002, Efficient large-scale underground utility mapping in New York City using a multi-channel ground-penetrating imaging radar system: Proc. of the SPIE, **4758**, 186-191.
- Birken, R., Hansen, T., Deming, R., and Oristaglio, M., 2004, Locating pipelines with a broadband electromagnetic induction array system: Proc. of SAGEEP 2004, Colorado Springs, Colorado.
- Burns, M., Derubeis, T., Albats, P., Casadonte, R., Birken, R., Deming, R., Haldorsen, J., Hansen, T., Miller, D.E., Oristaglio, M.L., 2004, Method for merging position information with measurements and filtering to obtain high-quality images that are positioned accurately with respect to global coordinates: United States patent 6,766,253.
- Conti, U., 1992, Multiple-coil magnetic field sensor with series-connected main coils and parallel-connected feedback coils: United States patent 5,130,655.
- Daniels, D. J., 1996, Surface-Penetrating Radar, IEE, Radar, Sonar, Navigation and Avionics Series 6, London.
- Hansen, T. and Johansen, P.M., 2000, Inversion scheme for ground penetrating radar that takes into account the planar air-soil interface: IEEE Geoscience and remote sensing, **38**, 1, 496-506.
- Jeong, H. S., Abraham, D.M., and Lew, J. J., 2003, Pipeline damage prevention systems: ASCE Conf. **130**, International Conference on Pipeline Engineering and Construction, M. Najafi (ed.), 1429-1427.
- Jeong, H. S., Abraham, D.M., and Lew, J. J., 2004, Evaluation of an emerging market in subsurface utility engineering: J. Construc. Eng. and Manufacturing, 130, 225-234.
- Johansson, B., 2002, Ground-penetrating radar array and timing circuits: US patent 6,496,137.
- Kalisch, B, 2000, Achieving Common Ground, AGA Special Report, www.aga.org.
- Lehmann, F. and Green, A.G., 1999, Semiautomated georadar acquisition system in three dimensions: Geophysics, **64**, 3, 710-731.
- Lew, J. J., 1996, Subsurface utility engineering – An initial step in project development, Proc., Associated Schools of Construction, Texas A&M Univ., College Station, Tex., 217-222.
- Lew, J. J. 2000, Cost savings on highway projects utilizing subsurface utility engineering: Federal Highway Administration, NTIS No. FHWA/IF00/014, Washington, D.C.
- Oristaglio, M., Miller, D.E. and Haldorsen, J., 2001, Ground Probing Radar, in Scattering, P. Sabatier and E. R. Pike (eds.), 1, chapter 1.6.4, Academic Press, London.
- Stevens, R. E., and Anspach, J. H., 1993, New technology overcomes the problem of underground system interferences on power projects, Proc., American Power Conf., Vol. 55, Illinois Institute of Technology, Chicago, 323-326.

Transportation Equity Act for the 21st Century, TEA 21, Title VII, Subtitle C, Comprehensive One-Call Notification, enacted June 9, 1998 (<http://www.fhwa.dot.gov/tea21/>).

Zembillas, N., 2003, Subsurface utility engineering – A technology-driven process that results in increased safety, fewer claims and lower costs, Proc., Conf of Int. Society of Trenchless Technologies (ISIT), CD-ROM, Copenhagen, Denmark.

Appendix A: U. S. DOT NEWS RELEASE



U.S. Department of Transportation
Office of Public Affairs
Washington, D.C.
www.dot.gov/affairs/briefing.htm

News

RSPA 26-02
Friday, November 15, 2002

Contacts: James Mitchell
Joe Delcambre
Tel.: (202) 366-4831

U.S. Department of Transportation (DOT) Awards \$1.6 Million for Pipeline Safety Research

U.S. Transportation Secretary Norman Y. Mineta today announced that the U.S. Department of Transportation (DOT) awarded seven research contracts totaling \$1.6 million to address pipeline damage prevention and leak detection solutions. These awards implement the first phase of a new competitive pipeline safety research partnership. DOT's awards provide approximately 50 percent of funding equal to \$1.6 million, for partnerships totaling \$3.4 million.

"By leveraging funding through partnerships, we expect to produce a wide range of research and stimulate the market with beneficial technologies two to three years sooner than would have otherwise been possible," said Secretary Mineta.

A government-industry leadership team that includes the U.S. Departments of Energy and Interior and several state agencies helped DOT build the blueprint for the new program and move from concept to award in one year. The partnership team reviewed over 85 applications submitted for the program's first phase. Moreover, the awards are for technologies that are ready for commercialization in three to five years, to move quickly to enhance pipeline safety. Awards for the second phase of the competitive program are pending.

"This is the first comprehensive public/private pipeline safety research program, co-funded by the department, universities and both the oil and natural gas industries," said Research and Special Programs Administrator Ellen G. Engleman. "It addresses the President's goal of advancing pipeline safety research and consolidating its management in the DOT for greater effectiveness."

The project awards are:

- Battelle Memorial Institute, Columbus, OH; Pipeline Research Council International, Inc., Washington, DC; Gas Technology Institute, Des Plaines, IL; and the ILI Technologies Corp., Calgary, Canada, to develop a simpler and smaller in-line inspection that detects and sizes metal loss (i.e. corrosion) and mechanical damage (\$380,000);

RSPA 26-02

Friday, November 15, 2002

- Southwest Research Institute, San Antonio, TX, and Pipeline Research Council International, Inc., Washington, DC, to modify in-line inspection tools to detect stress measurements that identify corrosion, mechanical damage, cracks, wrinkles, etc. (\$80,000);
- Southwest Research Institute, San Antonio, TX, and Pipeline Research Council International, Inc., Washington, DC, for alternative in-line inspection technologies that have potential to negotiate unpiggable pipelines (\$40,000);
- Southwest Research Institute, San Antonio, TX, and Pipeline Research Council International, Inc., Washington, DC, for testing remote field eddy current inspection system for unpiggable pipelines (\$87,500);
- Witten Technologies, New York, NY; ConEdison, New York, NY; and Electromagnetic Instruments, Inc., at University of California-Berkeley, CA, for development of a 3-D digital mapping system for detecting steel and plastic underground utilities and leaks (\$439,000);
- Gas Technology Institute, Des Plaines, IL, for development of locatable magnetic signature plastic gas pipe (\$95,500); and
- PetroChem Inspection Services, Houston, TX; Pennsylvania State University; and Plant Integrity LTD, Cambridge, United Kingdom, to improve long-range ultrasonic inspection technologies for use in detection of unpiggable pipelines (\$500,000)

RSPA has public responsibilities for safe and secure movement of hazardous materials to industry and consumers by all transportation modes, including the nation=s pipelines; rapid response to emergencies by government agencies; training for transportation safety professionals; and applying science and technology to meet national transportation needs.

For additional information, go to the RSPA website <http://primis.rspa.dot.gov/rd> or contact James.Mitchell@rspa.dot.gov or Gordon.Delcambre@rspa.dot.gov.

###

Appendix B: Utility Locating Markets: One-Call System and SUE

Utility Locating (One-Call)

Utility locating is a service consortium of companies that locate underground utilities before construction or digging. The consortium is organized under the One-Call (or “Call-Before-You-Dig”) system now mandated in the US. Full establishment of the One-Call system was contained in the *Transportation Equity Act for the 21st Century*, TEA 21, Title VII, Subtitle C, Comprehensive One-Call Notification, enacted June 9, 1998 (<http://www.fhwa.dot.gov/tea21/>).

“One-Call” refers to a single number published in phone books that will access the service for all buried utilities. A call to the system, which is required before any digging, generates a “locate ticket” that is dispatched to a service provider who sends a technician to the site to locate the buried lines and place appropriate markings on the ground. The service is free to the person making the call; its cost is built into utility rates.

Standards for One-Call locating are modest: surface markings must be within 1.5 feet of the horizontal location of buried utilities; depth is not required.

A survey of Standard Industrial Classification reveals over a dozen different kinds of companies active in this market. These include companies specializing in utility locating, construction or excavation companies, geophysical and engineering companies, and public or private utility companies.

One-Call is the largest market in underground mapping services, but is highly fragmented and regional. No single company has more than 10% of the market. Margins are low, and there is little differentiation in technology.

Utility locating markets have been growing steadily over the past decade, driven in part by legislation, but also by the need to avoid costly accidents. The SUE market has been growing the fastest. Within the next ten years it is possible that a combination of new legislation setting higher standards for One-Call, pressure from insurance companies to reduce liability by adopting “best practices”, and reduction in costs of 3D mapping will make SUE quality standards the norm for all utility locating. SUE would then encompass the entire multi-billion dollar utility locating market.

Several factors will drive this trend:

- Crowded Rights of Way — Underground rights of way are becoming crowded and competition for limited space is growing. The broadband “last mile” and maintenance of existing infrastructure in cities will demand high levels of construction in already dense utility corridors.
- Non-Conductive Utilities and Uncertainty in Locates — Buried utilities now include non-conductive materials, such as plastic, glass, and clay, which are nearly invisible to the metal detectors used to do most locating. Even conductive utilities, when densely packed, are vulnerable to misidentification with existing technology.
- Rising Damage Costs — Accidents continue to occur under the One-Call System. Accurate estimates of yearly damage are difficult to obtain, but insurance figures suggest it is in the range of several hundred million dollars yearly. (A GRI study reported that in 1993 damage to gas lines alone from digging accidents cost \$86 million.) Companies are pursuing recovery of these costs more vigorously. Use of SUE standards, especially Quality Level A, will increase safety margins.
- Need for Precision in Directional Drilling — Directional drilling (also called “trenchless technology”) is being used more and more to emplace utilities in crowded utility corridors. Planning and executing a directional drilling plan requires an accurate 3D map of existing lines and other possible obstructions.

- Lack of Permanent Records — One-Call locating services only provide temporary surface markings, which are later washed away or obscured. To avoid this waste, digital archiving of utility maps according to SUE standards is gradually being adopted by municipalities.

Subsurface Utility Engineering

Subsurface utility engineering (SUE) is a new discipline that uses advanced technology in site characterization and data management to collect and depict information about buried utilities (see, e.g., Anspach, 1995; Zembillas, 2003). The technologies involved include geophysical remote sensing, surveying and mapping, CAD and GIS. SUE engineers certify utility information in accordance with a standard classification scheme that allows a better allocation of risk between the project owner, project engineer, utility owner and construction manager. The end product is a complete utility map that is often integrated into the engineering design of a construction project.

The Federal Highway Administration (FHWA) has been promoting the use of SUE since 1987 as a means to save costs on highway construction projects. Some states, such as Virginia, now require SUE before any highway construction. A study commissioned by FHWA in 1996 examined 71 highway projects in four states and estimated savings of about \$23 million, or 2% on the total value of the construction (about \$1 billion), from use of SUE. Extrapolating to the \$59 billion estimated for highway construction in 2004 suggests a possible savings of over \$1 billion per year from systematic use of SUE across the US.

Today, SUE relies mainly on vacuum excavation to expose buried utilities with small “potholes” or “test pits” at sites selected by studying existing maps or by locating utilities with traditional (2D) geophysical methods. Location, depth, size and type of utility are recorded by hand. New maps are then created by extrapolating information between holes or by filling the gaps with 2D geophysical mapping along linear profiles at 10 to 20 feet spacing. SUE contracts usually require that final results adhere to one of four standard quality levels.

- *Quality Level D*: Information derived solely from existing records or verbal recollections.
- *Quality Level C*: Information obtained by surveying and plotting visible (above-ground) utility features and by using professional judgment in correlating this information to Quality Level D information.
- *Quality Level B*: Information obtained through the application of appropriate surface geophysical methods to identify the existence and approximate horizontal position of subsurface utilities. “Quality Level B” data are reproducible by surface geophysics at any point of their depiction. This information is surveyed to applicable tolerances and reduced onto plan documents.
- *Quality Level A*: Information obtained by the actual exposure (or verification of previously exposed and surveyed utilities) of subsurface utilities, using (typically) minimally intrusive excavation equipment to determine their precise horizontal and vertical positions, as well as their utility attributes. This information is surveyed and reduced onto plan documents. Accuracy is typically set at 15 mm (0.6 inch) vertical, and to applicable horizontal survey and mapping standards.

Subsurface Utility Engineering is among the fastest-growing markets in engineering services. SUE started in the late 1980s and reached about \$20 million annually by the early 1990s, promoted by a handful of companies and state DOTs. Since then, the market has been doubling about every 5 years and is currently about \$100 million per year, split among about 50 firms. Case law (on utility accidents), insurance practices and standards promoted by professional organizations, such as the American Society of Civil Engineers (ASCE), will continue to push SUE standards to improve safety and efficiency in underground construction. Estimates are that the market can reach \$1 billion within the next 5 to 10 years. Leading private SUE companies are So-Deep, Inc., which helped pioneer SUE in the late 1980s, and TBE Group, Inc. (formerly Tampa Bay Engineering). The So-Deep website (www.sodeep.com) is an excellent source of background material and project examples for SUE.

Appendix C – Physics of the dual-array system

Radar and induction methods for probing objects in the earth generate and detect classical electromagnetic fields described by solutions of Maxwell's equations in conductive media. This Appendix presents these solutions for simple models that illustrate the physics of the dual-array system. We assume that the reader is already familiar with basic concepts of electromagnetism and present only the key equations. Many general texts on electromagnetics and its applications cover this same ground at a more relaxed pace. Two excellent introductory texts are Kraus and Fleisch (1999) and Shen and Kong (1995); a more advanced text with emphasis on electromagnetic fields in the earth and other inhomogeneous media is Chew (1995). There is also a vast literature on radar and electromagnetic induction for remote sensing and non-destructive evaluation. A standard general reference for radar is Skolnick (1980). Daniels (1996) is still the most complete treatment of ground-penetrating radar technology, but is somewhat out of date (a new edition is due out in 2005); Oristaglio et al. (2001) is a brief modern review. The two-volume monograph edited by Nabighian (1988) is the most comprehensive reference on geophysical applications of electromagnetic induction methods.

Notation and conventions

We will develop Maxwell's equations for electromagnetic fields varying harmonically (sinusoidally) in time at a fixed frequency, represented by the general form,

$$A(\mathbf{r}, t) = \mathcal{R}e \{ A(\mathbf{r}, \omega) e^{-i\omega t} \} \quad (\text{C-1})$$

where $A(\mathbf{r}, t)$ is a real function giving the amplitude of a field component at location \mathbf{r} and time t ; $A(\mathbf{r}, \omega)$ is the complex harmonic field amplitude at angular frequency ω ; $i = \sqrt{-1}$; and $\mathcal{R}e \{ \}$ indicates the real part of the quantity in braces. Angular frequency $\omega = 2\pi f$, where f is the frequency in cycles per second (Hz). Any physical field varying in time can be represented as a sum (or integral) of harmonic components. We use Cartesian coordinates with position vector $\mathbf{r} = x\hat{\mathbf{x}} + y\hat{\mathbf{y}} + z\hat{\mathbf{z}}$, where $\{\hat{\mathbf{x}}, \hat{\mathbf{y}}, \hat{\mathbf{z}}\}$ are unit vectors in the coordinate directions, and (x, y, z) are the coordinates of \mathbf{r} . (Boldface indicates vectors.) The length of the position vector (the distance from the origin) is $r = |\mathbf{r}| = \sqrt{x^2 + y^2 + z^2}$, while $\hat{\mathbf{r}} = \mathbf{r}/r$ is a unit vector in the direction pointing to \mathbf{r} . We will use the coordinate z to represent depth in the earth, as shown in Figure C-1. Finally, ∇ is the vector differential operator

$$\nabla = \hat{\mathbf{x}} \frac{\partial}{\partial x} + \hat{\mathbf{y}} \frac{\partial}{\partial y} + \hat{\mathbf{z}} \frac{\partial}{\partial z} .$$

Maxwell's equations

Maxwell's equations for the complex electric field $\mathbf{E}(\mathbf{r}, \omega)$ and magnetic field $\mathbf{B}(\mathbf{r}, \omega)$ vectors are

$$\nabla \times \mathbf{E} = i\omega \mathbf{B}, \quad (\text{C-2})$$

$$\nabla \times \mathbf{B}/\mu = (\sigma - i\omega\epsilon)\mathbf{E} + \mathbf{J}_s, \quad (\text{C-3})$$

where the sources of the time-varying EM fields are impressed currents, represented by the current density \mathbf{J}_s . In radar, the impressed currents are on the transmitting antenna that broadcasts the pulse of radio

waves; in induction, the impressed currents are on the loops of wire in the “clamp-on” or “on-board” transmitter that generates the primary magnetic field.

The electrical properties of the subsurface – the soil and buried objects – are given by the electrical permittivity ϵ , conductivity σ , and permeability μ . In the most general anisotropic medium, these properties can all be tensor functions of position and frequency (\mathbf{r}, ω) . We will assume for simplicity that electrical anisotropy is negligible – ϵ , σ , and μ are then scalar quantities – and that μ assumes its free-space value $\mu_0 = 4\pi \times 10^{-7}$ ohm-s/m, which holds for most soils. (Exceptions are certain magnetic soils, derived from weathering of volcanic or other rocks with high concentrations of iron-rich minerals, which have a large magnetic permeability. See, e.g., Dabas et al., 1992.) It is also convenient to write $\epsilon = \epsilon_0 \epsilon_r$, where $\epsilon_0 = 8.85 \times 10^{-12}$ s/ohm-m is the permittivity of free-space and ϵ_r is the medium’s relative permittivity, usually called its (relative) “dielectric constant”. The dielectric constant of most soils is in the range from 2 to 16, whereas the conductivity varies from nearly zero in dry sandy soils to about 0.1 S/m in wet clays. Both of these properties are influenced strongly by the amount of saline water present in the soil, usually either filling the pore space between grains or adhering to clay particles making up the grains. FIGURE C-2 illustrates the strong influence that water content has on the electrical properties of a type of soil called sandy-clay “loam”. Values of conductivity are sometimes given in terms of its inverse, the resistivity, $\rho = 1/\sigma$. The resistivity of most soils is in the range from 10 to 10 000 ohm-m.

The term $(\sigma - i\omega\epsilon)\mathbf{E}$ in the second of Maxwell’s equations represents secondary electrical currents that flow in material media in response to the electric field \mathbf{E} . These currents in the soil or other buried objects, such as pipes, are the physical sources of the radar echoes detected by GPR and of the secondary magnetic fields measured by an induction system. Secondary currents consist of both conduction currents ($\sigma\mathbf{E}$) and displacement ($-i\omega\epsilon\mathbf{E}$) currents. The different physics of radar and induction methods, as described in the text, depends mainly on the relative size of the displacement and conduction currents in the soil. As shown below, wavelike propagation dominates when $\omega\epsilon \gg \sigma$; diffusive behavior, when $\omega\epsilon \ll \sigma$. The frequency at which these quantities are equal is usually called the “corner frequency” f_c , which is at the transition between diffusive and wavelike behavior. In a soil with conductivity 0.02 S/m and dielectric constant of 9, which are typical values for moist sandy-clay soils, the corner frequency is about 40 MHz. These properties are illustrated in the models developed in the next two sections.

Plane-wave solutions: Propagation, decay, and diffusion

Maxwell’s equations (C-2) and (C-3) combine to give the vector “wave” equation,

$$\nabla \times \nabla \times \mathbf{E} - k^2(\omega)\mathbf{E} = i\omega\mu\mathbf{J}_s, \quad (\text{C-4})$$

where $k^2 = \omega^2\mu\epsilon + i\omega\mu\sigma$. In regions outside the source, equation (C-4) has plane-wave solutions of the form,

$$\mathbf{E}(\mathbf{r}, \omega) \sim \mathbf{E}_o e^{i\mathbf{k}\cdot\mathbf{r}}, \quad (\text{C-5})$$

where \mathbf{k} is a complex propagation vector and \mathbf{E}_o is a complex amplitude vector, subject to

$$\mathbf{k} \cdot \mathbf{k} = k^2 = \omega^2\mu\epsilon + i\omega\mu\sigma; \quad \mathbf{E}_o \cdot \mathbf{k} = 0. \quad (\text{C-6})$$

Assume that the plane wave travels along the z -axis (“depth”), and is polarized along the y -direction; then the electric field is given by

$$\mathbf{E}(\mathbf{r}, \omega) = \hat{\mathbf{y}} E_y(z, \omega) = \hat{\mathbf{y}} E_o e^{ikz}, \quad (\text{C-7})$$

where

$$k = k_R + ik_I = \omega \sqrt{\mu\epsilon} \left(1 + i \frac{\sigma}{\omega\epsilon}\right)^{1/2} \quad (\text{C-8})$$

is the wave's complex propagation constant and E_o is its (real) amplitude at the surface $z = 0$. In general, solution (C-7) describes a wave which propagates at phase velocity ω/k_R and decays at the rate k_I in the positive z -direction (when $k_R, k_I, \omega > 0$ and time-dependence $e^{-i\omega t}$ is restored).

Radar

The expression for the propagation constant simplifies considerably in the two frequency regimes where either conduction or displacement currents dominate. Consider, first, the radar regime at frequencies where $\sigma/\omega\epsilon \ll 1$. The propagation constant is then given by

$$k \approx \omega \sqrt{\mu\epsilon} \left(1 + i \frac{\sigma}{2\omega\epsilon}\right) = \frac{\omega}{c} + i\alpha, \quad (\text{C-9})$$

with

$$c = \frac{1}{\sqrt{\mu\epsilon}} = \frac{c_0}{n}, \quad \text{and} \quad (\text{C-10})$$

$$\alpha = \frac{\sigma}{2} \sqrt{\frac{\mu}{\epsilon}} = \frac{\eta_0 \sigma}{2n}, \quad (\text{C-11})$$

where $c_0 = (\mu_0\epsilon_0)^{-1/2}$ is the speed of light in free-space, $n = \sqrt{\epsilon_r}$, and $\eta_0 = (\mu_0/\epsilon_0)^{1/2} \approx 377$ ohm is the impedance of free-space. The full form of the field as a function of depth and time is then

$$E_y(z, t) = \mathcal{R}e \left\{ E_o e^{-\alpha z} e^{i\omega z/c} e^{-i\omega t} \right\} = E_o e^{-\alpha z} \cos \omega(z/c - t), \quad (\text{C-12})$$

which represents a sinusoidal wave that travels with speed $c = c_0/n$ in the positive z direction and attenuates exponentially in this direction at the rate α . Both the speed and attenuation rate are independent of frequency in the radar regime, which means that a superposition of harmonic waves of different frequencies – for example, a radar pulse – retains its shape. The quantity $n = \sqrt{\epsilon_r}$ is the medium's index of refraction. Equations (C-11) and (C-12) give formula (6) in the text for the radar attenuation rate in soil

Induction

In the diffusive regime where conduction currents dominate, $\omega\epsilon/\sigma \ll 1$, the term $\omega^2\mu\epsilon$ can be ignored in the expression for the propagation constant, giving,

$$k \approx \sqrt{i\omega\mu\sigma} = (1+i)\alpha', \quad (\text{C-13})$$

where

$$\alpha' = \sqrt{\frac{\omega\mu\sigma}{2}}. \quad (\text{C-14})$$

The form of the solution is then

$$E_y(z, t) = E_o e^{-\alpha' z} \cos \omega(z/c' - t), \quad (\text{C-15})$$

where

$$c' = \sqrt{\frac{2\omega}{\sigma\mu}}. \quad (\text{C-16})$$

is the (phase) velocity of the harmonic wave. The key feature of the diffusive regime is that the attenuation rate and speed of harmonic plane waves depend on frequency, with both varying as $\omega^{1/2}$. In particular, the exponential attenuation can be reduced to any desired rate by lowering the frequency. Equations (C-14) and (C-15) give formula (7) in the text for the attenuation rate of induction signals in soil. This rate is sometimes given in terms of its inverse,

$$\delta = 1/\alpha' = \sqrt{\frac{2}{\omega\mu\sigma}} \approx 503.3\sqrt{\frac{\rho}{f}}, \quad (\text{C-17})$$

called the “skin depth”, which is the distance over which the amplitude of a plane wave in the medium decays to $e^{-1} \approx .37$ (or -8.7 dB) of its initial value.

Antennas and transmitters

The electromagnetic field radiated by a GPR antenna or by current flowing along a short length of wire in an inductive transmitter is modelled to a very good approximation by the field of an electric dipole. Moreover, the field of an arbitrary (impressed or secondary) distribution of current can always be represented as a superposition of current dipoles. To study this solution, let the dipole be at the origin of coordinates and pointing in the y -direction (FIGURE C-1, middle). Then, the electric field satisfies the vector wave equation,

$$\nabla \times \nabla \times \mathbf{E} - k^2(\omega)\mathbf{E} = \hat{y} i\omega\mu\bar{I}(\omega)\delta(\mathbf{r}), \quad (\text{C-18})$$

where $\bar{I}(\omega)$ is the current moment of the dipole in units of amp-m (a current dipole is the idealization of current I flowing along a short length of wire dl).

The vector electric field of the dipole is most simply expressed in spherical coordinates (r, θ, ϕ) around the axis of the dipole (FIGURE C-1, middle): r is the distance from the dipole to the observation point, θ is the angle between the dipole axis and the radius vector \mathbf{r} , and ϕ is the azimuthal angle – in this case, the angle measured clockwise between the x -axis and projection of \mathbf{r} onto the (x, z) -plane. Note that this clockwise convention for the azimuthal angle ϕ changes the sign of certain field components compared to the standard counterclockwise convention. The non-zero field components are

$$\mathbf{B}(\mathbf{r}, \omega) = B_\phi \hat{\phi}, \quad \text{and} \quad \mathbf{E}(\mathbf{r}, \omega) = E_r \hat{r} + E_\theta \hat{\theta}, \quad (\text{C-19})$$

where $(\hat{r}, \hat{\phi}, \hat{\theta})$ are unit vectors in the spherical coordinate directions. The components are given by

$$B_\phi = -\mu\bar{I}(\omega) \left(-ik + \frac{1}{r} \right) \frac{e^{ikr}}{4\pi r} \sin \theta, \quad (\text{C-20})$$

$$E_\theta = -i\omega\mu\bar{I}(\omega) \left(1 + \frac{i}{kr} - \frac{1}{k^2r^2} \right) \frac{e^{ikr}}{4\pi r} \sin \theta, \quad (\text{C-21})$$

$$E_r = -i\omega\mu\bar{I}(\omega) \left(\frac{2i}{kr} - \frac{2}{k^2r^2} \right) \frac{e^{ikr}}{4\pi r} \cos \theta. \quad (\text{C-22})$$

As shown below, these solutions illustrate the behavior of radar and inductive methods with realistic sources.

Radar in conductive and non-conductive soil

The electric field given by equations (C-21) and C-22) is a good approximation to the field of a GPR antenna lying on the surface of the earth. These expressions do not include effects at the earth-air interface, but the main effect of the interface is just to alter (moderately) the amplitude of the field radiated in different directions into the ground. When the field is measured in the $(x, 0, z)$ -plane (i.e., in the plane $\theta = 90^\circ$ perpendicular to the axis of the dipole), the electric field has only a component perpendicular to the (x, z) -plane (i.e., in the y -direction), which is given by

$$E_y(\mathbf{r}, \omega) = i\omega\mu\bar{I}(\omega) \left(1 + \frac{i}{kR} - \frac{1}{k^2R^2}\right) \frac{e^{ikR}}{4\pi R}, \quad (\text{C-23})$$

where $\mathbf{r} = x\hat{\mathbf{x}} + z\hat{\mathbf{z}}$, and $R = \sqrt{x^2 + z^2}$ (FIGURE C-2, right). At large distances from the source, where $|kR| \gg 1$, the first term dominates, giving the classical radiation field

$$E_y(\mathbf{r}, \omega) \approx i\omega\mu\bar{I}(\omega) \frac{e^{ikR}}{4\pi R}. \quad (\text{C-24})$$

We can use equation (C-23) to illustrate the difference between radar in non-conductive and in conductive soil by computing the pulse that is radiated when the current on the source is switched on and off with a given waveform, which is how most modern GPRs operate. The full time-dependent field is an integral superposition of harmonic solutions,

$$E_y(\mathbf{r}, t) = \mathcal{R}e \left\{ \frac{1}{\pi} \int_0^\infty E_y(\mathbf{r}, \omega) e^{-i\omega t} d\omega \right\}. \quad (\text{C-25})$$

In conductive media, the integral must be evaluated numerically. The example in FIGURE C-3 shows the evolution from the near to far field in a wholespace with relative dielectric $\epsilon_r = 9$, a typical value for sandy-clay soils, corresponding to a speed of light of 0.1 m/ns (an index of refraction of 3). Waveforms are shown for soils in which the conductivity increases from 0 to 0.05 S/m (a relatively conductive soil). The source current is the first derivative of a gaussian function with a central frequency of about 200 MHz. The wavelength in the non-conductive soil at the central frequency of the source is about 0.5 m.

Consider first the non-conductive soil (the left panel of FIGURE C-3). In the near field, the propagated waveform is a combination of the source current and its integral, whereas in the far field the waveform is proportional to the time-derivative of the current waveform with the propagation delay R/c ,

$$E_y(\mathbf{r}, t) \approx -\frac{\mu}{4\pi R} \bar{I}'(t - R/c), \quad (R \rightarrow \infty), \quad (\text{C-26})$$

which follows from (C-24). ($\bar{I}' = d\bar{I}/dt$.) The far-field approximation is already accurate to a few per cent at a distance of only 1.5 m from the source, which is about 3 wavelengths at the central frequency of the waveform.

In conductive soil, the wave is attenuated and distorted as it propagates. This can be seen by comparing the waveforms in the left and right panels of FIGURE C-3. In particular, at the distance of 5 m from the source in the conductive soil, there is a long tail of diffusive energy in the waveform, which arises because the central frequency (200 MHz) is right at the corner frequency of the transition from diffusive to wavelike behavior in this soil with a conductivity of 0.05 S/m and a dielectric constant of 9.

The middle panel shows waveforms in soil of conductivity 0.02 S/m. In this case, $\omega\epsilon/\sigma \gg 1$ in the effective bandwidth of the source current, and the distortion of the waveform is negligible. The main effect in the far field is an exponential attenuation of the signal,

$$E_y(\mathbf{r}, t) \approx -\frac{\mu e^{-\alpha R}}{4\pi R} I'(t - R/c), \quad (R \rightarrow \infty), \quad (\text{C-27})$$

where $\alpha = \sigma\mu c/2 = \sigma\eta_0/2n$. (The actual attenuation is accurately given by equation C-27, but is not visible in the figure because each waveform has been normalized to the same level for better comparison of the shapes.) Equation (C-27) is perhaps the most important single equation in GPR and can be used to derive many other results, including formulas for synthetic-aperture GPR imaging (Oristaglio et al., 2001) and estimates for the depth to which GPR can detect buried objects (see below).

Magnetic fields of the dipole and line current

The most useful model for understanding the direct, or clamp-on, inductive method described in the text is the field of an infinite line of current, which is a good approximation to the field set up when current is injected onto a long metal pipe in soil. The field of a line current can be obtained by integrating the magnetic field of the electric dipole,

$$B_\phi = -\mu\bar{I}(\omega) \left(-ik + \frac{1}{R} \right) \frac{e^{ikR}}{4\pi R} \sin\theta,$$

from $y = -\infty$ to $+\infty$. Note first that, in the limit of steady current ($\omega = 0$), this expression reduces to

$$B_\phi = -\frac{\mu I dl}{4\pi R^2} \sin\theta, \quad \text{or} \quad \mathbf{B} = \frac{\mu I d\mathbf{l} \times \hat{\mathbf{r}}}{4\pi R^2}, \quad (\omega = 0), \quad (\text{C-28})$$

which is the standard Biot-Savart law for the magnetic field of a steady current I along a short wire dl .

Integrating first the Biot-Savart formula over a line current gives the well-known expression for the field of an infinite steady current,

$$B_\phi = -\frac{\mu I}{2\pi R}, \quad (\text{C-29})$$

which is probably the single most useful formula for understanding the clamp-on method. For example, this expression gives the following formulas for the magnetic field at the surface of the earth along a profile perpendicular to the axis of a pipe at depth z (FIGURE C-4):

$$B_x = -\frac{\mu I}{2\pi} \frac{z}{x^2 + z^2}, \quad \text{and} \quad B_z = -\frac{\mu I}{2\pi} \frac{x}{x^2 + z^2}. \quad (\text{C-30})$$

These expressions for the magnetic field of a steady current hold for any finite conductivity of the soil and show clearly that the magnitude of the horizontal magnetic field peaks directly above the pipe, whereas the vertical magnetic field goes through zero (a null).

The magnetic field of a long linear current at a finite frequency is given by integrating the dipole field (C-20), which gives

$$B_\phi = \frac{\mu k I}{4i} H_1(kR) \quad (\text{C-31})$$

where H_1 is the first-order Hankel function of the first kind. This formula is not easy to analyze directly, because there is no simple general expression for the Hankel function. But for large and small values of kR , it has the following limiting forms,

$$H_1(kR) \approx \frac{-2i}{\pi kR}, \quad (kR \rightarrow 0); \quad (\text{C-32})$$

$$H_1(kR) \approx \sqrt{\frac{2}{\pi}} \frac{e^{ikR - i\pi/4}}{\sqrt{kR}}, \quad (kR \rightarrow \infty). \quad (\text{C-33})$$

The first of these equations reproduces the static limit (C-29), as $\omega \rightarrow 0$. The second equation determines the decay rate of the magnetic field at large distances from the current in a conductive medium, which ultimately sets the detection limit for the clamp-on method. The plots in FIGURE C-5 compare the exact solution (C-31) for a current at 32 kHz with the static limit for a pipe at a depth of 5 m in soils of different conductivity. The static limit is very accurate at shallow depths and low conductivities and is the basis of the inversion method developed for the EMI array. The analysis in Appendix D shows that the accuracy of the static limit is not changed significantly by the earth-air interface.

Guidelines for depth of penetration of radar and induction methods

This section uses the simple models of the previous sections to estimate the depth of investigation of radar and induction methods in conductive soil. These estimates are rough guidelines that capture the essential physics of electromagnetic fields in the ground. The actual depth of investigation of these methods will depend on many factors, including the hardware used (e.g., the size, shape, and efficiency of radar antennas) and the detailed characteristics of the site (such as the composition of the roadbed overlying the soil). These complications usually reduce the depth of investigation, so figures derived here are best viewed as upper limits.

GPR range equation

The model shown in FIGURE 1 can be used to develop an approximate range equation for GPR. The model assumes that the transmitting and receiving antennas are close together, directly above a pipe at depth z in the soil. If the pipe is in the far field (we are looking for the maximum range of the radar), the following expression, based on equations (C-27) and (C-11), is a reasonable model for the amplitude of the returned echo,

$$A_e = \left(\frac{e^{-\alpha z}}{z} \right) R_{cs} \left(A_o \frac{e^{-\alpha z}}{z} \right) = R_{cs} A_o \frac{e^{-\eta_0 \sigma z/n}}{z^2}, \quad (\text{C-34})$$

where A_o is the amplitude of the wave transmitted into the ground; $\eta_0 \approx 377$ ohm is the impedance of free-space; σ and n are the conductivity and index of refraction of the soil; and R_{cs} is the radar “cross section” of the pipe, which is a measure of its ability to generate a radar echo. (R_{cs} has units of m^2 .) The three terms in the first part of equation (C-34) represent (from right to left) propagation from the transmitter to the pipe, reflection at the pipe, and propagation back to the receiving antenna. The condition for detecting the echo is that the amplitude ratio A_e/A_o should be within the dynamic range of the system; that is,

$$20 \log_{10}(A_e/A_o) = 20 \left(\log_{10} R_{cs} - 2 \log_{10} z - 0.4343 \frac{\eta_0 \sigma}{n} z \right) > dB_S, \quad (\text{C-35})$$

where dB_S is the system's dynamic range (in dB).

According to equation (C-35), the depth of penetration of radar increases as the soil's electrical conductivity decreases (its resistivity increases) and as its index of refraction increases. If the soil's properties do not vary with frequency, the range equation is independent of frequency and there is no trade-off between frequency and depth of penetration involving the soil's properties. In principle, this feature would generally favor use of the highest frequency radar available (because higher frequencies have better resolution). In practice, the electrical conductivity of moist soils increases gradually with frequency through the MHz range, mainly because the conductivity of water is increasing at these frequencies. The index of refraction is relatively constant over the same range of frequencies. FIGURE C-2 illustrates this effect for sandy-clay loams. The increase of conductivity with frequency decreases the depth of penetration of GPR at higher frequencies in the MHz range. Properties of the radar system, such as antenna efficiency and dynamic range, can also vary with frequency causing depth of penetration to vary – e.g., the efficiency of electronics generally decreases with frequency in this range.

Parameters

The conductivity of typical sandy-clay soils found in the northeastern United States ranges from about 0.01 S/m to 0.05 S/m (equivalent to resistivities from 100 to 20 ohm-m). The index of refraction of nearly all soils falls in the range from 1.4 to 6 (equivalent to dielectric constants from about 2 to 36). Typical ranges for soils in the New York metropolitan area are σ from 0.02 to 0.04 S/m and n from 3 to 4.

The radar cross section R_{cs} is the most difficult quantity to estimate in equation (C-34). R_{cs} depends on the contrast in electrical properties (σ and ϵ_r) between the soil and object, the size and shape of the object, and its internal composition. Metal objects will have higher radar cross sections than other objects of similar size, because the conductivity of metals is many orders of magnitude higher than that of soil. Plastic, ceramic, or cement can also have a large radar cross section because their dielectric properties will be different from soil (although in the same general range). Water has one of the largest dielectric constants of any material – about 80 in the frequency range of GPR – which also makes it a strong radar scatterer. The best way to determine R_{cs} , along with other system parameters that can determine the performance of GPR, is by calibrating the radar in a test pit.

FIGURE C-6 illustrates the GPR range equation, calibrated by measurements made with a 200 MHz CART system. The maximum and minimum signals that could be recorded by early versions of the CART system were about 15 000 and 100, respectively (in arbitrary units). The dynamic range of the recorded amplitudes was thus about 1:150 (-44 dB). The dynamic range of the CART's analog-to-digital converter is actually 60 dB, but the recorded dynamic range was limited by system noise. A controlled test with a metal pipe, 8-inches in diameter at a depth of 1.2 m (4 ft) in dry sand ($\sigma \approx 0$; $n = 4$), determined a value for R_{cs} of about 1 m² for this type of pipe. The curves in FIGURE C-6 show that the same pipe could be detected at depths of 0.5, 0.8, 1.2, and 2.5 m in soils with resistivities of 15, 30, and 60, and 120 ohm-m, respectively. Increasing the system's dynamic range to its ideal limit (-60 dB) increases these depths to 0.7, 1.3, 2.2, and 3.6 m.

Range of the inductive clamp-on method

Equation (C-31) can be used to estimate the range of the inductive clamp-on method, under the assumption that current is injected onto a long linear pipe at depth. The curves in FIGURE C-7 show the amplitude of the magnetic field directly above a pipe in soils of different resistivity as the depth of the pipe increases. The pipe carries 0.001 A of current at 32 kHz; the value 0 dB represents a field of 1 nT. The red dotted line in the figure is the minimum magnetic field detectable at 32 kHz by the induction coil sensors in the EMI array, which is about 10^{-4} nT or -80 dB. As the curves show, the EMI sensors can detect 1 mA of current along pipes at depths of 50 m or more even in very conductive soils, which illustrates the long range of the EMI array in the ideal system limit. In practice, background magnetic-field “noise”, coming from natural or man-made sources, can limit the ability of sensors to detect small magnetic fields. For example, the green dotted line shows the natural magnetic-field noise in a 1 kHz bandwidth centered on 32 kHz, which is about 0.0003 nT (-70 dB on the scale used for the plot), or three times the system noise. In principle, background noise can be eliminated, or reduced significantly, by averaging the measurement over many cycles of the transmitter.

REFERENCES

- Chew, W., 1995, *Waves and Fields in Inhomogeneous Media*, IEEE Press, New York.
- Dabas, M., Jolivet, J., and Tabbagh, A., 1992, Magnetic susceptibility and viscosity of soils in a weak time varying field, *Geophysical Journal International*, **108**, 101-109.
- Daniels, D. J., 1996, *Surface-Penetrating Radar*, Institution of Electrical Engineers, London.
- Hipp, J. E., 1974, Soil electromagnetic parameters as functions of frequency, soil density, and soil moisture: *Proc. IEEE*, **62**, 98–103.
- Kraus, J. D., and Fleisch, D., 1999, *Electromagnetics*, 5th ed., Mc-Graw Hill.
- Nabighian, M.N., ed., 1988, *Electromagnetic Methods in Applied Geophysics*, Tulsa, Society of Exploration Geophysicists, 2 volumes.
- Oristaglio, M., Miller, D.E., and Haldorsen, J., 2001, Ground Probing Radar, in *Scattering*, P. Sabatier and E. R. Pike (eds.), v. 1, chapter 1.6.4, 448–466, Academic Press, London.
- Shen, L., and Kong, J.-A., 1995, *Applied Electromagnetism*, 3rd ed., Thomson-Engineering.
- Skolnik, M. I., 1980, *Introduction to Radar Systems*, 2nd ed., McGraw-Hill.
- Wang, T., and Oristaglio, M., 2000, Simulation of GPR surveys over pipes in dispersive soils, *Geophysics*, **65**, 1560-1568.

Appendix D: CART Imaging System

The radar unit intended for use in the dual-array system is an array ground-penetrating radar (GPR), developed from 1997 to 2002 by Witten Technologies, Malå Geoscience AB, Dycom Industries, Inc., and Schlumberger Limited. Some of the development, mainly of the data processing and imaging software, was carried out in a project at Schlumberger that was partly sponsored by the Electric Power Research Institute (Bernstein et al., 2000; Birken et al., 2002). The system is marketed by Malå, Witten Technologies, and their licensees under the brand name *CART Imaging System* (CART stands for “computer assisted radar tomography”). The radar hardware is currently built exclusively by Malå; Witten Technologies provides a full range of software for the system, including software for the positioning system; for data processing and image analysis; and for creation of final maps in CAD. Witten Technologies has exclusive licensing rights for uses of the CART system in mapping buried utilities.

This Appendix describes briefly the technical specifications and operation of the CART system. For a general discussion of modern GPR equipment and its uses, Daniels (1996) is still the most comprehensive reference, although it is somewhat out-of-date for today’s hardware (a new edition is due to be published in 2005). Oristaglio et al. (2001) is a concise review, including modern imaging theory and applications.

When introduced in 2000, the CART was the first commercial array GPR with the capability of creating 3D synthetic-aperture underground images over large areas. The system has 9 transmitters and 8 receivers in two parallel rows (FIGURE 3). In normal operation, the radar data acquisition system – usually called the radar “controller” – creates 16 independent GPR channels by firing each transmitter twice and recording radargrams in turn at each of the transmitter’s two neighboring receivers (Johansson, 2002). For example, as illustrated in FIGURE 3, channels 8 and 9 are created by firing transmitter T5 twice and recording a radargram first at receiver R4 and then at receiver R5.

The separations between antennas are such that the radargram from each transmitter-receiver pair can be treated as a “zero-offset” recording at the pair’s midpoint – i.e., as if the transmitter and receiver were located at the same point, halfway between their actual locations. This zero-offset approximation is not fundamental, but does simplify data processing. The CART system can also operate in a much-slower mode in which each transmitter fires sequentially into all 8 receivers, creating 72 independent GPR channels at a range of different offsets.

Like all modern GPRs, the CART is an ultra-wideband (UWB) radar that broadcasts a narrow pulse of radio-wave energy with significant frequency content away from the “peak” frequency (the frequency at which the pulse has maximum energy). The CART has two different sets of bow-tie antennas (FIGURE 3): one set has a peak frequency of about 200 MHz and a (zero-offset) channel spacing of about 14 cm; the other set has a peak frequency of about 400 MHz and a channel spacing of 8 cm. FIGURE 3 shows a typical pulse shape and spectrum for the 200 MHz antennas. The pulse lasts for about 5 ns and has a bandwidth (at the -20 dB points) extending from about 50 MHz to 450 MHz; i.e., the bandwidth is equal to twice (200% of) the peak frequency. By comparison, in a typical narrowband radar, such as those used in air-traffic control, the bandwidth is only a few percent of the peak frequency.

The CART is a “stepped-time” radar. The transmitter has to fire many times to generate each radargram, because the digitizing electronics are not fast enough to record more than one sample at a time at one receiver (see, e.g., Johansson, 2002, and Oristaglio et al., 2001, for a description of how the timing circuitry works). The source fires at the rate of 100 kHz (one shot every .01 ms). To record a radargram consisting of 256 samples (e.g., 25.6 ns at 0.1 ns sampling), the source fires 256 times – in other words recording one radargram requires about 2.56 ms. All 16 channels are collected in about 40 ms. The system has a timing accuracy of about 0.05 ns.

Other specifications of the CART system are shown in TABLE D-1. Full operation of the system is described in Birken et al. (2002).

Recently, array units have become available from other manufacturers, including the following:

- Terravision from GSSI (www.geophysical.com), and
- GeoScope from the Norwegian company 3-D Radar, Inc. (www.3d-radar.com/products/)

The GSSI system is also used by Guardian ProStar under its service name Digital Dig (www.guardianprostar.com/digitaldig.html).

Although there are differences in the hardware specifications for these systems, the array GPRs all operate along similar lines.

TABLE D-1. CART Imaging System Technical Specifications

Type of radar	Ultra-wideband impulse ("stepped-time" data recording)	
Antennas	Broadband shielded bow-tie: 9 Tx, 8 Rx	
Tx-Rx channels (zero-offset)	16	
Timing resolution and Firing Rate	0.05 ns at 100 kHz firing rate	
Linear Coverage Rate (maximum)	3.3 ft/s (2.2 mi per hr) with 4 in sampling in profile direction 1 m/s (3.6 km per hr) with 10 cm sampling in profile direction	
Data acquisition rate	16 radargrams, 256 samples each, in approx. 40 ms	
Tracking Accuracy	+/- (0.01 ft + 2 ppm) up to 656 ft; +/- (3 mm + 3 ppm) up to 200 m +/- (0.016 ft + 3 ppm) beyond 656 ft; +/- (5 mm + 3ppm) beyond 200 m	
Dynamic range	60 dB (theoretical); 44 dB (maximum signal/system noise level)	
Power Supply	12V DC	
Output Power	Approx. 20 mW average	
	200 MHz CART	400 MHz CART
Frequency Bandwidth	50 MHz to 400 MHz	100 to 650 MHz
Channel spacing (cross-line)	5.25 inches (13.4. cm)	3.25 in (8.25 cm)
Depth of penetration	About 6 ft (1.6 m)	About 4 ft (1.2 m)
Location Accuracy (of an imaged feature)	+/- 5% in depth +/- 2% in horizontal position	+/- 5% in depth +/- 2% in horizontal position

Appendix E: Inversion models for inductive pipe locating

This appendix describes the inversion models and algorithms used to invert measurements of the vector magnetic field at the earth's surface, as recorded by the sensors in the EMI array, to obtain the approximate locations and depths of buried pipes. Different models are used for the “clamp-on” and “on-board transmitters”. In this appendix, we work the magnetic field vector $\mathbf{H} = \mathbf{B}/\mu$ where μ is the magnetic permeability. In all cases, we assume that μ is equal to its free-space value $\mu_0 = 4\pi \times 10^{-7}$ ohm-s/m.

Pipe location with clamp-on source

Assume that one or more signal generators (the transmitters) operating in the kHz range inject currents onto one or more pipes in the subsurface (the primary pipes). The transmitters can be connected (clamped on) to the pipes in manholes, test pits, or at locations above the surface where the pipes are accessible (e.g. some water pipes are accessible at fire hydrants). The currents on the primary pipes induce additional currents in the soil and on nearby pipes (the secondary pipes). The total currents in the subsurface emit a magnetic field that is measured above ground with the array system to get a “digital map” of the magnetic field at each of the transmitter frequencies. In this appendix we develop a method to determine the locations of both the primary and secondary pipes from such digital maps of the magnetic field.

We begin by showing that in the frequency range from 100 Hz to 100 kHz, the spatial dependence of the total magnetic field from the currents that flow on the buried pipes and in the soil is approximately the same as the spatial dependence of the magnetic field due to “fictitious” static line currents that flow along the pipes. Consider a y -directed line source with strength I_0 buried in soil. The regions $z > 0$ and $z < 0$ are air and soil, respectively, and the line source passes through the point $(x, y, z) = (x_0, 0, z_0)$ with $z_0 < 0$. Air is assumed to have the electrical properties of vacuum, so that its permittivity and permeability are ϵ_0 and μ_0 . The permittivity, permeability, and conductivity of soil are $\epsilon_s = \epsilon_r \epsilon_0$, $\mu_s = \mu_r \mu_0$, and σ , respectively. With $e^{-i\omega t}$ time dependence suppressed, the exact magnetic field in air at $(x, y, z) = (x, 0, h)$, $h > 0$ is given in terms of plane waves by the standard expression [3, Ch.2]

$$\mathbf{H}(x, 0, h) = \frac{I_0}{2\pi} \int_{-\infty}^{+\infty} \frac{\gamma_0 \hat{\mathbf{x}} - k_x \hat{\mathbf{z}}}{\gamma_0 + \gamma_s} e^{i(k_x(x-x_0) - \gamma_s z_0 + \gamma_0 h)} dk_x \quad (\text{E-1})$$

where $\gamma_0 = \sqrt{k_0^2 - k_x^2}$ and $\gamma_s = \sqrt{k_s^2 - k_x^2}$ have non-negative real and imaginary parts. Moreover, $k_0 = \omega\sqrt{\epsilon_0\mu_0}$ and $k_s = \sqrt{\omega^2\epsilon_s\mu_s + i\omega\sigma\mu_s}$ are the propagation constants in air and soil, respectively. The formula (E-1) takes into account currents in the soil and is valid all the way from statics to the wave regime (GHz). We shall use formulas throughout the paper that hold also in the wave regime since they are no more complicated than formulas valid only in the diffusive regime (kHz). The static magnetic field that corresponds to (E-1) is simply

$$\mathbf{H}(x, 0, h) = \frac{I_0}{2\pi} \frac{(h - z_0)\hat{\mathbf{x}} - (x - x_0)\hat{\mathbf{z}}}{(x - x_0)^2 + (h - z_0)^2}. \quad (\text{E-2})$$

FIGURE E-1 shows the comparison between the exact magnetic field (E-1) and the static magnetic field (E-2) for $I_0 = 1$ A, $x_0 = 0$, $z_0 = -1$ m, $h = 0.3$ m, $\sigma = 0.05$ S/m, $\epsilon_r = 9$, and $\mu_r = 1$ at the frequencies 10 kHz and 100 kHz. (At these frequencies the permittivities are unimportant since displacement currents

are negligible.) The static formula approximates the exact magnetic field well. The shape of the curves are the same and an almost perfect match could be obtained (even at 100 kHz) by adjusting the strength of the static current. Hence, we shall use static line currents to model the actual kHz currents induced on the buried pipes.

The method for determining the pipe locations from the recordings of the magnetic field consists of three steps:

1. Based on the recorded magnetic fields, a static current model is constructed in which the currents flow along piecewise straight line segments. The model parameters are the current strengths and coordinates of the endpoints of the line segments. The currents vary linearly along each line segment.
2. A cost function is defined that measures the difference between the recorded magnetic field and the magnetic field of the static current model.
3. An iterative optimization method determines the model parameter values that minimize the cost function. The resulting parameter values determine the approximate locations of the buried pipes.

The iterative optimization method requires that the magnetic field of the model be computed at all receiver locations for many different positions of the static currents. Hence, to make the method feasible it is necessary to have rapidly-calculable formulas for the magnetic field of static line currents. In the last section, we derive a closed-form expression for the magnetic field of a tapered static line current that begins at \mathbf{r}_a and ends at \mathbf{r}_b . The current strength varies linearly from the value I_a at \mathbf{r}_a to the value I_b at \mathbf{r}_b . The magnetic field of this current is denoted by $\mathbf{H}^s(\mathbf{r}; I_a, I_b, \mathbf{r}_a, \mathbf{r}_b)$ and given by (E-19) in Appendix C. Throughout the paper, $\mathbf{r} = x\hat{\mathbf{x}} + y\hat{\mathbf{y}} + z\hat{\mathbf{z}}$ is a general point in space.

A single pipe in the subsurface can often be represented well by a chain of such straight lines with tapered currents. At the node points where two line segments meet, the current strengths are required to be continuous. The decay of the current strength along the pipe is due to leakage of current into the surrounding soil and onto nearby pipes. Assume that the chain has N_c links determined by $N_c + 1$ current-segment endpoints. Let the endpoints be given by \mathbf{r}_p and the corresponding current values by I_p , where $p = 1, 2, 3, \dots, N_c + 1$. The magnetic field at \mathbf{r}_0 due to this chain of currents is then

$$\mathbf{H}^{s,chain}(\mathbf{r}_0; I_1, I_2, \dots, I_{N_c+1}, \mathbf{r}_1, \mathbf{r}_2, \dots, \mathbf{r}_{N_c+1}) = \sum_{p=1}^{N_c} \mathbf{H}^s(\mathbf{r}_0; I_p, I_{p+1}, \mathbf{r}_p, \mathbf{r}_{p+1}) \quad (\text{E-3})$$

where \mathbf{H}^s is given by (E-19). With this model the current is guaranteed to be continuous along the chain, except possibly at the two endpoints. A network of buried pipes can be represented by multiple chains of line currents. Complicated junctions can also be represented with this type of model. The condition that the total current that flows towards a junction equals the total current that flows away from a junction is imposed at junctions where more than two pipes meet.

Based on the recorded magnetic field, an approximate model for the pipes in the subsurface is constructed. Let this model consist of N pieces of line current and let the end points of these be given by \mathbf{r}_{ap} and \mathbf{r}_{bp} with $p = 1, 2, 3, \dots, N$. The corresponding current strengths are I_{ap} and I_{bp} . If the model consists of one or more current chains, some of the endpoints and current strengths satisfy continuity requirements: $\mathbf{r}_{bq} = \mathbf{r}_{aq+1}$ and $I_{bq} = I_{aq+1}$.

Assume that the magnitude H_x of the x component of the magnetic field has been measured at the points \mathbf{r}_j , $j = 1, 2, \dots, M$ above the surface. A cost function for the x component of the magnetic field can then be computed as

$$C_x(\mathbf{r}_{a1}, \mathbf{r}_{a2}, \dots, \mathbf{r}_{aN}, \mathbf{r}_{b1}, \mathbf{r}_{b2}, \dots, \mathbf{r}_{bN}, I_{a1}, I_{a2}, \dots, I_{aN}, I_{b1}, I_{b2}, \dots, I_{bN}) \\ = \sum_{j=1}^M \left| \left| \sum_{p=1}^N H_x^s(\mathbf{r}_j; \mathbf{r}_{ap}, \mathbf{r}_{bp}, I_{ap}, I_{bp}) \right| - H_x(\mathbf{r}_j) \right|^\beta \quad (\text{E-4})$$

where β is a positive constant and H_x^s is the x component of the magnetic field in (E-19). The cost function is large when the magnetic field of the model is significantly different from the measured magnetic field. A small value of the cost function is achieved when the magnetic field of the model matches the measured magnetic field well.

Similar cost functions are computed for other rectangular components of the magnetic field that may be measured. A total cost function is obtained by combining the cost functions for each of the rectangular components of the magnetic field.

The endpoints \mathbf{r}_{ap} and \mathbf{r}_{bp} and the currents I_{ap} and I_{bp} must now be determined such that the cost functions are minimized and the static model currents closely follow the currents that flow on the real pipes. The minimization can be achieved with the Newton optimization schemes in the MATLAB Optimization Toolbox. The location of the buried pipes are obtained by drawing straight lines between the set of endpoints \mathbf{r}_{ap} and \mathbf{r}_{bp} that minimizes the cost function. Through numerical experimentation we found it useful in some cases to constrain (fix) certain of the model parameters so that they cannot be varied by the optimization scheme. Thus, the number of free parameters is reduced. Typically, one can constrain one of the coordinates of each node point for a single pipe.

At this stage it is worth mentioning the commercially available equipment most often used for locating pipes. The clamp-on transmitter of the commercial equipment is identical to the one we use with the inductive array. The receiver is typically hand-held and measures two magnetic field components at a few selected frequencies. The pipe location is determined from the formula (E-2) for the magnetic field of an infinite line current. First the user determines the lateral position of the pipe x_0 by moving the hand-held receiver over the ground until a maximum of H_x or a null of H_z is found. Then, the horizontal magnetic field component perpendicular to the pipe is recorded at two heights to obtain two equations for determining the two remaining unknowns I_0 and z_0 . These equations are solved with a built-in processor. The depth estimates obtained this way are very sensitive to noise because they rely on only two magnetic field measurements and are invalid when more than one pipe is present.

Pipe location with on-board source

The clamp-on configuration described in the previous appedix can be used only if part of the pipe is exposed, so that a signal can be injected. Moreover, for large street surveys the clamp-on points must be changed as the receiver array moves out of range. This may significantly slow down the survey because most pipes in urban environments can only be accessed through manholes. These disadvantages of the clamp-on method can be overcome if the transmitter rides with the receiver array and transmits the signals to the pipes through air and soil. Hence, the “on-board” transmitter configuration considered in this appendix makes surveying easier.

The on-board transmitter rides with the receiver array, so the induced currents on the pipes change as the receiver array moves. Therefore, the method developed in Appendix A for determining the pipe locations from clamp-on data does not immediately apply. Fortunately, we can augment the clamp-on method to allow the currents on the pipes to change with receiver position to obtain a method that applies to on-board data. For this method to be useful, we must find a way to rapidly compute the induced currents on a general pipe configuration for a large number of transmitter locations. (We have already shown in Appendix A how to rapidly compute the magnetic fields given the currents on the pipes.)

To compute the induced currents on the pipes, we begin by considering the incident field in the soil. As in Appendix A, $z > 0$ is air and $z < 0$ is homogeneous soil. We first assume that the on-board transmitter is a circular horizontal loop with N_l windings, current strength I_l , and radius a_l located at $\mathbf{r}_T = x_T \hat{\mathbf{x}} + y_T \hat{\mathbf{y}} + z_T \hat{\mathbf{z}}$ above the air-soil interface. At the end of this appendix we discuss arbitrary transmitter sources. The incident field at the point \mathbf{r} in the soil is then

$$\mathbf{E}^i(\mathbf{r}, \mathbf{r}_T) = -\hat{\phi}_T \omega \mu_0 N_l I_l a_l^2 \int_0^\infty \frac{J_1(k_\rho a_l)}{k_\rho a_l} \frac{k_\rho^2 J_1(k_\rho \rho_T) e^{i(z_T \gamma_0 - z \gamma_s)}}{\gamma_0 + \gamma_s} dk_\rho \quad (\text{E-5})$$

which can be obtained easily from a formulation of plane-wave theory for layered media that employs rectangular field components [1]. Here $\rho_T = \sqrt{(x - x_T)^2 + (y - y_T)^2}$, $\hat{\phi}_T = [-(y - y_T)\hat{\mathbf{x}} + (x - x_T)\hat{\mathbf{y}}]/\rho_T$, and J_1 is the Bessel function of order one. All other parameters are defined in Appendix A.

Numerical studies show that when the loop radius is small the incident field (E-5) can be approximated well by the field of a magnetic dipole situated in a homogeneous soil region. Hence, we can write

$$\mathbf{E}^i(\mathbf{r}, \mathbf{r}_T) = \hat{\phi}_T \frac{e^{ik_s r_T}}{r_T} \frac{\rho_T}{r_T} \left[1 + \frac{i}{k_s r_T} \right] F(\rho_T, z, z_T) \quad (\text{E-6})$$

where $r_T = \sqrt{\rho_T^2 + (z - z_T)^2}$ is the distance from the dipole to the observation point and $F(\rho_T, z, z_T)$ is a slowly-varying function that can be approximated well by a rapidly-calculable function. A good approximation is $F(\rho_T, z, z_T) \equiv \text{constant}$. The incident field that illuminates the pipes can thus be computed easily.

We approximate the induced current at the point \mathbf{r} on the pipe by the Born-Kirchhoff type expression

$$I(\mathbf{r}, \mathbf{r}_T, \alpha) = \alpha \hat{\mathbf{s}} \cdot \mathbf{E}^i(\mathbf{r}, \mathbf{r}_T) \quad (\text{E-7})$$

where $\hat{\mathbf{s}}$ is the unit tangent vector to the pipe and α is a constant that depends on the pipe and soil. At points where the tangent jumps from $\hat{\mathbf{s}}_1$ to $\hat{\mathbf{s}}_2$, we replace $\hat{\mathbf{s}}$ in (E-7) by the “average” tangent $(\hat{\mathbf{s}}_1 + \hat{\mathbf{s}}_2)/|\hat{\mathbf{s}}_1 + \hat{\mathbf{s}}_2|$. If the pipe is perfectly conducting, straight, infinitely long, and the incident field is a plane

wave whose variation over a pipe cross section is negligible, the expression (E-7) becomes exact if we let $\alpha = 4\sqrt{(\epsilon_s + i\sigma_s/\omega)/\mu_s}/H_0^{(1)}(k_s a)$, where a is the pipe radius and $H_0^{(1)}$ is the Hankel function of the first kind and order zero.

Having determined the induced currents for each transmitter location, the results of Appendix A show that the magnetic field from a chain of N_c straight line currents with endpoints \mathbf{r}_p can be approximated by

$$\mathbf{H}^P(\mathbf{r}_R, \mathbf{r}_T; \mathbf{r}_1, \mathbf{r}_2, \dots, \mathbf{r}_{N_c+1}, \alpha) = \sum_{p=1}^{N_c} \mathbf{H}^S(\mathbf{r}_R; I(\mathbf{r}_p, \mathbf{r}_T, \alpha), I(\mathbf{r}_{p+1}, \mathbf{r}_T, \alpha), \mathbf{r}_p, \mathbf{r}_{p+1}) \quad (\text{E-8})$$

where \mathbf{H}^S is the field of a tapered static current given by (E-19), and \mathbf{r}_R is the receiver location. The expression (E-8) can be generalized straightforwardly to allow the constant α in the current expression (E-7) to vary along the chain. The node points \mathbf{r}_p should be spaced close enough to ensure that the current (E-7) can be approximated well by a linear function between two node points.

In addition to the magnetic field emanating from the currents on the buried pipes, the receiver array senses the direct field from the transmitter current loop and the reflected field from the soil-filled half space. The direct field is [2, Eq.(2.335)]

$$\mathbf{H}^D(\mathbf{r}_R, \mathbf{r}_T) = \frac{N_l I_l a_l}{4\pi} \int_0^{2\pi} (1 - ik_0 R) \hat{\phi}' \times \mathbf{R} \frac{e^{ik_0 R}}{R^3} d\phi' \quad (\text{E-9})$$

where $\hat{\phi}' = -\sin \phi' \hat{\mathbf{x}} + \cos \phi' \hat{\mathbf{y}}$, $\mathbf{R} = (x_R - x_T - a_l \cos \phi') \hat{\mathbf{x}} + (y_R - y_T - a_l \sin \phi') \hat{\mathbf{y}} + (z_R - z_T) \hat{\mathbf{z}}$, and $R = |\mathbf{R}|$. From the plane-wave formulation in [1] we find that the reflected field is

$$\mathbf{H}^R(\mathbf{r}_R, \mathbf{r}_T) = \frac{N_l I_l a_l^2}{2} \int_0^{\infty} \frac{J_1(k_\rho a_l)}{k_\rho a_l} \frac{\gamma_0 - \gamma_s}{\gamma_0 + \gamma_s} \left[J_1(k_\rho \rho_{TR}) \hat{\rho}_{TR} + \frac{ik_\rho}{\gamma_0} \hat{\mathbf{z}} \right] e^{i\gamma_0(z_R + z_T)} k_\rho^2 dk_\rho \quad (\text{E-10})$$

where $\rho_{TR} = \sqrt{(x_R - x_T)^2 + (y_R - y_T)^2}$ and $\hat{\rho}_{TR} = [(x_R - x_T) \hat{\mathbf{x}} + (y_R - y_T) \hat{\mathbf{y}}] / \rho_{TR}$. The total model magnetic field at the receiver location \mathbf{r}_R is the sum of the three fields (E-8), (E-9), and (E-10):

$$\mathbf{H}^M(\mathbf{r}_R, \mathbf{r}_T; \mathbf{r}_1, \mathbf{r}_2, \dots, \mathbf{r}_{N_c+1}, \alpha) = \mathbf{H}^P(\mathbf{r}_R, \mathbf{r}_T; \mathbf{r}_1, \mathbf{r}_2, \dots, \mathbf{r}_{N_c+1}, \alpha) + \mathbf{H}^D(\mathbf{r}_R, \mathbf{r}_T) + \mathbf{H}^R(\mathbf{r}_R, \mathbf{r}_T). \quad (\text{E-11})$$

We can express each receiver position as $\mathbf{r}_R = \mathbf{r}_T + \Delta$, where Δ is an offset vector unique to that receiver. Since the background field $\mathbf{H}^D(\mathbf{r}_D, \mathbf{r}_T) + \mathbf{H}^R(\mathbf{r}_R, \mathbf{r}_T)$ does not change as the receiver array moves over the ground (provided the soil does not change), the expressions (E-9) and (E-10) need only be calculated once for each receiver. In practice one can avoid using (E-9) and (E-10) altogether by setting the background field at each receiver equal to an unknown complex constant, which then becomes part of the parameter set for the model. The problem of determining the pipe locations is now reduced to minimizing a cost function similar to (E-4).

At kHz frequencies the propagation constant for air is on the order of 10^{-4} m^{-1} , so the phase of the direct field in (E-9) is approximately the same as the phase of the transmitter current. The strong direct transmitter signal therefore is present only in the in-phase component of the received magnetic field and absent from the quadrature component. The magnetic field generated by the induced current on a buried pipe will in general be much smaller than the direct field, but contribute to both in-phase and quadrature

components of the received field. Therefore, it is advantageous to define the cost function in terms of quadrature components only.

Let us finally discuss other transmitters than the horizontal loop that was used in the derivation. Only the formulas (E-5), (E-6), (E-9), and (E-10) depend on the transmitter. Expressions for the incident electric field in the soil and the reflected field from the air-soil interface can easily be obtained for arbitrary transmitters by employing plane-wave formulas, which give the spectra explicitly as simple integrations over source currents [1]. The direct field is obtainable from the usual expression for the magnetic field of a current. The only remaining task is to determine a rapidly-calculable expression (like (E-6)) for the incident electric field in the soil. Such an expression can often be derived by multiplying the solution to a simpler source problem by a slowly-varying function (like $F(\rho_T, z, z_T)$ in (E-6)) that can be tabulated.

Straight line with tapered current

We first consider the auxiliary problem in which the line current begins at the origin and ends at $(x, y, z) = (0, 0, L)$. Here, $L > 0$ is the length of the line current. The current strength is given by the linear expression $I(z) = I_0 + (I_L - I_0)z/L$ where I_0 and I_L are constants. In standard cylindrical coordinates (ρ, ϕ, z) , symmetry ensures that only the ϕ component of the magnetic field of this current is nonzero. We denote this ϕ component by \tilde{H}_ϕ^s and have [2, Eq. (4.50)]

$$\begin{aligned}\tilde{H}_\phi^s(\rho, z; I_0, I_L, L) &= \frac{\rho}{4\pi} \int_0^L \frac{I_0 + (I_L - I_0)z'/L}{[\rho^2 + (z - z')^2]^{3/2}} dz' \\ &= \frac{I_0 + (I_L - I_0)z/L}{4\pi\rho} \left[\frac{L - z}{\sqrt{\rho^2 + (L - z)^2}} + \frac{z}{\sqrt{\rho^2 + z^2}} \right] \\ &\quad - \frac{(I_L - I_0)\rho/L}{4\pi} \left[\frac{1}{\sqrt{\rho^2 + (L - z)^2}} - \frac{1}{\sqrt{\rho^2 + z^2}} \right]\end{aligned}\quad (\text{E-12})$$

where $\rho = \sqrt{x^2 + y^2}$. The superscript s indicates that the magnetic field is “synthetic” (not a measured field). Note that \tilde{H}_ϕ^s is independent of ϕ . The formula (E-12) simplifies considerably when the current strength is constant ($I_L = I_0$).

We shall now determine the magnetic field of the general line current that is located in the lower half space $z < 0$ and extends from \mathbf{r}_a to \mathbf{r}_b . The current varies linearly as $I(s) = I_a + (I_b - I_a)s/|\mathbf{r}_b - \mathbf{r}_a|$, where s is the arclength of the line. The constants I_a and I_b are the current values at the endpoints of the line current. The parameter s is chosen such that $s = 0$ corresponds to the point \mathbf{r}_a and $s = |\mathbf{r}_b - \mathbf{r}_a|$ corresponds to the point \mathbf{r}_b . The magnetic field of this line current is given by a complicated expression [2, Eq. (4.50)]:

$$\mathbf{H}^s(\mathbf{r}; I_a, I_b, \mathbf{r}_a, \mathbf{r}_b) = \frac{1}{4\pi} \int_0^{|\mathbf{r}_b - \mathbf{r}_a|} I(s') \frac{\mathbf{r}_b - \mathbf{r}_a}{|\mathbf{r}_b - \mathbf{r}_a|} \times \frac{\mathbf{r} - \mathbf{r}'}{|\mathbf{r} - \mathbf{r}'|^3} ds'. \quad (\text{E-13})$$

Instead of attempting to evaluate (E-13) directly, we use the expression (E-12) for \tilde{H}_ϕ^s along with a coordinate transformation that converts the problem of the general line current into the simpler problem solved by (E-12).

We define a new coordinate system (x', y', z') with its origin at \mathbf{r}_a and its z' unit vector given by

$$\hat{\mathbf{z}}' = \frac{\mathbf{r}_b - \mathbf{r}_a}{|\mathbf{r}_b - \mathbf{r}_a|}. \quad (\text{E-14})$$

Hence, the z' axis passes through the line current and is given in the (x, y, z) coordinate system by the expression $\mathbf{r}_c(z') = \mathbf{r}_a + z'\hat{\mathbf{z}}'$. Note that $z' = s$, where s is the parameter used above in the expression for the current $I(s)$.

The magnetic field at an arbitrary point \mathbf{r}_0 can be expressed in terms of \tilde{H}_ϕ^s in (E-12) if (i) the coordinates (ρ'_0, z'_0) are known, and (ii) the $\hat{\mathbf{x}}$, $\hat{\mathbf{y}}$, and $\hat{\mathbf{z}}$ components of the unit vector $\hat{\phi}'_0$ are known. Here the subscript zero indicates that the quantities are evaluated at \mathbf{r}_0 .

The coordinate z'_0 is determined by the equation $[\mathbf{r}_c(z'_0) - \mathbf{r}_0] \cdot \hat{\mathbf{z}}' = 0$, which can be solved to get

$$z'_0 = \hat{\mathbf{z}}' \cdot [\mathbf{r}_0 - \mathbf{r}_a]. \quad (\text{E-15})$$

The vector that extends from the point z'_0 on the z' axis to \mathbf{r}_0 is simply

$$\begin{aligned}\boldsymbol{\rho}'_0 &= \mathbf{r}_0 - \mathbf{r}_c(z'_0) \\ &= [\mathbf{r}_0 - \mathbf{r}_a] \cdot [\bar{\mathbf{I}} - \hat{\mathbf{z}}'\hat{\mathbf{z}}']\end{aligned}\quad (\text{E-16})$$

where $\bar{\mathbf{I}}$ is the identity dyad. Hence,

$$\rho'_0 = \left| [\mathbf{r}_0 - \mathbf{r}_a] \cdot [\bar{\mathbf{I}} - \hat{\mathbf{z}}'\hat{\mathbf{z}}'] \right|.\quad (\text{E-17})$$

We also have $\hat{\boldsymbol{\phi}}'_0 = \hat{\mathbf{z}}' \times \hat{\boldsymbol{\rho}}'_0$, which becomes

$$\hat{\boldsymbol{\phi}}'_0 = \frac{1}{\rho'_0} \hat{\mathbf{z}}' \times \left([\mathbf{r}_0 - \mathbf{r}_a] \cdot [\bar{\mathbf{I}} - \hat{\mathbf{z}}'\hat{\mathbf{z}}'] \right)\quad (\text{E-18})$$

The final expression for the magnetic field of the line current is then

$$\mathbf{H}^s(\mathbf{r}_0; I_a, I_b, \mathbf{r}_a, \mathbf{r}_b) = \hat{\boldsymbol{\phi}}'_0 \tilde{H}_\phi^s(\rho'_0, z'_0; I_a, I_b, |\mathbf{r}_b - \mathbf{r}_a|).\quad (\text{E-19})$$

References

- [1] T.B. Hansen and P. Meincke, "Scattering from a buried circular cylinder illuminated by a three-dimensional source," *Radio Science*, v. 37, no. 2, March-April 2002, pp.1-23.
- [2] T.B. Hansen and A.D. Yaghjian, *Plane-Wave Theory of Time-Domain Fields*, New York: IEEE Press, 1999.
- [3] W.C. Chew, *Waves and Fields in Inhomogeneous Media*, New York: IEEE Press, 1995.

Appendix F: Data File Formats

TABLE 10: Overview of File Formats used in Dual Array System			
File Names and Extensions	File Format	Description	Creator
.rad	ascii	radar header file	GPR
.rd3	binary	radar data file	GPR
.ssf	trimble	GPS raw data file	GPS
.cor	trimble	differentially corrected GPS data	GPS
.pos	ascii	exported GPS data	GPS
.inf	ascii	header file for exported GPS data	GPS
.att	ascii	feature description file for exported GPS data	GPS
.dat	ascii	reformated (exported) GPS data	Data Extract
.raw	ascii	Total Station data file	Total Station
.airh	ascii	AIR header file	AIR
.aird	binary	AIR data file	AIR
geo.mat	mat	combined geometry data for GPR	Matlab(GPR)
.gpih	mat	processed radar data header file	Matlab(GPR)
.gpil	binary	processed radar data file	Matlab(GPR)
freq_extract.mat	mat	extracted frequency data for AIR	Matlab(AIR)
geo_air.mat	mat	combined geometry data for AIR	Matlab(AIR)
pi_*.mat	mat	pipe file for AIR/GPR	Matlab(AIR/GPR)
.mov	mpeg	movie of 3D radar images	QuickTime
.tiff	tiff	image files imported into AutoCAD MAP	Matlab(AIR)
.jpg	jpg	image files imported into AutoCAD	Matlab(GPR)
.scr	ascii	script files used to import images (tiff and jpg) into AutoCAD(MAP)	Matlab(GPR)
.mxd	ESRI	ESRI ArcMap document	ArcGIS
.aux, .tfw, .tif	ESRI	tif images and world files	ArcGIS
.dbf, .shp, .shx	ESRI	shape files	ArcGIS
.dwg	CAD	layered image file	AutoCad (MAP)
.dgn	CAD	layered image file	Microstation
.pdf	Adobe	portable data format	Adobe Acrobat